

Contents lists available at ScienceDirect

Energy

journal homepage: www.elsevier.com/locate/energy





Surrogate-enhanced multi-objective optimization of on-board hydrogen production device for carbon-free heavy-duty vehicles

Hao Zhang ^{a,c,2}, Jiaxi Xu ^{b,1,2}, Nuo Lei ^{c,*}, Bingbing Li ^a, Hao Sun ^a, Boli Chen ^{a,**}

- ^a Department of Electronic and Electrical Engineering, University College London, London, WC1E 6BT, UK
- ^b Department of Physics and Astronomy, University College London, London, WC1E 6BT, UK
- ^c School of Vehicle and Mobility, Tsinghua University, Beijing, 100084, China

ARTICLE INFO

Handling Editor: Prof X Ou

Keywords: Ammonia decomposition Ammonia-hydrogen powertrains Dual-phase optimization Partitioned exploration Surrogate model

ABSTRACT

The design of on-board ammonia decomposition units (ADUs) and its integration with ammonia-hydrogen hybrid powertrains present a critical challenge in the development of carbon-free heavy-duty vehicles. This study addresses this challenge through a novel surrogate-enhanced optimization framework for ADU design, introducing a dual-phase hybrid optimization framework combining non-dominated sorting genetic algorithm for partitioned exploration and Bayesian optimization for local refinement. The framework employs sequential domain decomposition using genetic algorithm-driven Pareto sampling integrated with surrogate training data accumulation, followed by Gaussian process-guided refinement that fuses adjacent optimal regions through covariance-based surrogate merging. Experimental validation demonstrates the effectiveness of the framework in achieving balanced system performance in key metrics. The results show that the powertrain equipped with the optimized ADU achieves a system efficiency of 31.24 % and an ADU efficiency of 76 % at minimal system costs, with dynamic validation more than 3.5 %.

Nomenclature (continued)

				NSGA-	Non-dominated Sorting	k_p^{α}	Differential factor
ICE	Internal combustion engine	P_{dem}	Power required under full	III	Genetic Algorithm III	•	
			loading	BO	Bayesian Optimization	P_{ele}^{dri}	Power provided by
ADU	Ammonia Decomposition unit	P_{DM}	Power provided by Ele			ete	electrical generator
EMS	Energy management system	P_{ICE}	Internal combustion engine power	SBX	Simulated Binary Crossover	Q_{Ele}	Heat transfer to electrical generator
TMS	Thermal management system	P_{bat}	Battery power	GP	Gaussian Process	Q_{ICE}^{exh}	Heat transfer to the engine
LHV	Lower heating value	P_{aux}	Auxiliary devices power			-IGE	exhaust gas
SOC	State of charge	T_{ADU}	Temperature of ADU	EI	Expected Improvement	ω_{ICE}	Engine speed
GHSV	Gaseous hourly space velocity	T_{cat}	Temperature of catalysts	P_{tot}^{dri}	Final drive power	T_{ICE}	Tenmperature of ICE
DRL	Deep Reinforcement Learning	η_{GEN}	Efficiency of electrical generator	$Q_{physical}$	Energy required for physical heating	$K_d^{\underline{FC}}$	Differential factor
RCCI	Reactivity Controlled Compression Ignition	η_{DM}	Efficiency of drive motor	T_{ICE}^{cool}	Fuel cell/engine coolant temperature	$Q_{chemical}$	Energy required for chemical heating
PEMFC	Proton exchange membrane fuel cells	η_f	Efficiency of final drive	Eff_{ADU}	Efficiency of ammonia decomposition unit	C_{steel}	Steel heat capacity
FLC	Fuzzy logic control	v_{ref}	Integral factor	$ ho_{H_2}$	Density of hydrogen	m_{H_2}	Mass of hydrogen
			(continued on next column)	$\rho_{N\!H_3}$	Density of ammonia	m_{NH_3}	Mass of ammonia
							(continued on next page)

^{*} Corresponding author.

https://doi.org/10.1016/j.energy.2025.137369

^{**} Corresponding author. Department of Electronic and Electrical Engineering, University College London, London, WC1E 7JE, UK. E-mail address: boli.chen@ucl.ac.uk (B. Chen).

¹ Co-first author.

 $^{^2}$ Jiaxi Xu and Dr. Hao Zhang contributed equally to the work and should be regarded as co-first authors.

(continued)

$a_{mix}^{\frac{v}{m}}$	Volume/mass ratio of the mixed gas	$m_{\stackrel{ADU}{ICE}}$	Mass of ADU/ICE
E_{ICE}^{rea}	Decomposition reaction energy in ICE	c_{ICE}	Engine specific heat capacity
S_i	The ith non-overlapping subregion	P_{merged}	The merged Pareto set
S_j	The jth subregion	$\mu_i(\mathbf{x})$	the mean function
P_j	The population for the jth subregion	x_{next}	The next evaluation point
F(x)	The objective vector	P_{GEN}^{max}	The max power of electrical generator
Z_r	Predefined reference point	f_i	The objective associated with system cost

1. Introduction

Excessive greenhouse gas emissions have led to an annual increase in global surface temperatures, exhibiting an exponential growth trend [1]. To achieve environmental sustainability goals, zero-carbon emissions have become the core focus of global long-term policies [2,3]. Since the signing of the Paris Agreement in 2015, over 100 countries have committed to achieving carbon neutrality in the coming decades [4]. In the composition of carbon emissions, road transport fossil fuel combustion contributes 23 % of CO2 emissions, with this proportion continuing to rise [5]. Moreover, heavy-duty trucks account for 76.1 % of nitrogen oxide emissions and 51.5 % of particulate matter emissions in the automotive sector [6], highlighting the urgency of commercial vehicle energy transition. However, current electric heavy-duty trucks are limited to short-distance transport due to range constraints [7], while liquid ammonia, with its volumetric energy density of 13.6 MJ/L, equivalent to 4.5 times that of 35 MPa high-pressure hydrogen [8], positions ammonia-hydrogen hybrid powertrains as the most promising zero-carbon solution for long-haul heavy-duty transport [9,10]. However, the complexity of system configuration and matching remains the primary bottleneck for commercialization.

Despite the significant potential of ammonia-hydrogen hybrid powertrains, the complexity of system configuration and matching has become the foremost obstacle to their commercialization. The multienergy source characteristics of such systems introduce technical integration challenges far exceeding those of single-power systems [11]. The dynamic matching of powertrain architectures becomes particularly intricate in ammonia-hydrogen powertrains. For example, Antonio et al. compared parallel, series, and power-split hybrid configurations, revealing that zero-carbon engines require real-time mode switching based on load conditions but exhibit vulnerable torque characteristics and significant emission increases under transient conditions, with improper system matching potentially causing substantial performance degradation [12]. Zhang et al. quantitatively studied the operation of ammonia-hydrogen hybrid powertrains under various working conditions through system modeling [13]. Their results demonstrated that while the system achieves significant carbon emission reductions compared to diesel hybrid heavy trucks and conventional diesel vehicles, the energy flow and parameter configuration exhibit limited adaptability to diverse operating conditions, leaving substantial optimization potential [14]. Therefore, it is obvious that the core challenge in ammonia-hydrogen system configuration lies in achieving synergistic optimization across conflicting objectives including enhancing system efficiency, minimizing powertrain weight, optimizing catalytic hydrogen production capacity, and reducing system cost.

Existing literature predominantly focuses on multi-objective sizing optimization schemes for conventional hybrid electric vehicles, proposing numerous valuable design methodologies from perspectives of optimization algorithms and system dynamics [15–18]. Zhang et al. developed a data-driven framework for online identification of fuel cell aging states, proposing a component matching and sizing architecture that considers system degradation [16]. Li et al. incorporated full

lifecycle carbon emission costs into powertrain component sizing optimization, creating decision-support models with enhanced industrial relevance for OEMs, though parameter accuracy remains a critical limitation [6]. Furthermore, recent advances in powertrain sizing leverage multi-objective optimization frameworks to address the interplay between component configuration, energy efficiency, and dynamic performance [19]. Evolutionary algorithms, such as non-dominated sorting genetic algorithm-III (NSGA-III) and reference-point-based methods, have demonstrated efficacy in resolving high-dimensional tradeoffs among cost, emissions, and energy density [20]. Hybrid approaches integrating surrogate models, such as polynomial chaos expansion, with metaheuristics enable efficient exploration of nonlinear design spaces while mitigating computational burdens [21]. For transient-aware sizing, physics-informed neural networks and digital twin frameworks are emerging to reconcile static parameter selection with real-world dynamic constraints [22]. Current challenges persist in balancing model fidelity with optimization scalability, particularly for multi-energy systems requiring concurrent sizing of electrochemical, thermal, and mechanical subsystems. Lei et al. adopted a hierarchical co-optimization architecture that simulates powertrain operating conditions to obtain dynamic feedback, effectively reducing temporal data errors across components [23]. Their system employed high-fidelity model integration techniques for multi-scale modeling, utilizing physical models like the Arrhenius combustion equation for cross-scale data fusion. Adaptive relaxation methods dynamically adjusted parameter conflicts, while surrogate models assisted in co-optimizing component sizing and energy management, achieving improvements in fuel economy and computational efficiency.

Despite over more than a decade of extensive research on hybrid powertrain matching, effective solutions remain lacking since the emergence of the novel complex coupling characteristics of ammoniahydrogen hybrid powertrains. To this end, Ezzat et al. investigated the co-optimization of system component sizing and energy management in ammonia-hydrogen vehicles, simultaneously determining component dimensions and optimizing the power distribution ratio between fuel cells and internal combustion engines (ICEs) [24]. Beyond computational simulations, some studies have developed design methodologies for small-scale ammonia-hydrogen systems, validated through golf cart prototypes [25], though their relevance to heavy-duty trucks with vastly different system scales remains limited. Notably, these studies neglect optimization of a critical component, the on-board hydrogen production unit namely ADU, and fail to address the co-optimization between ADU and other system components. Ammonia decomposition can generally be classified into thermal and non-thermal processes, with thermal decomposition further divided into three different methods: combustion heating, electric heating, and solar heating. This paper focuses on combustion heating for ammonia decomposition. Combustion heating can be flame combustion or catalytic combustion, with catalytic combustion being the process used in the ADU for ammonia hydrogenation. The rate of catalytic decomposition in the ADU, as well as key parameters, such as hydrogen conversion rates, are highly dependent on the properties of the catalyst. Active components of the catalyst can be combined with multiple metals or converted into carbides, nitrides, or amides to achieve more ideal properties. Additionally, the active components can be supported on different materials or encapsulated within various substances. For example, ruthenium (Ru) is often used as a carbon-supported catalyst, where the carbon support improves the dispersion of the precious metal Ru, thereby controlling the overall preparation cost. The structure of the catalyst, through controlling the number and distribution of active sites, also enhances the stability of the catalyst. Research demonstrates that Ru-based catalysts achieve 99.5 % ammonia decomposition at 500 °C [26,27], but at 20 times the cost of Fe/Co/Ni catalysts [28]. While non-precious metal catalysts offer cost advantages, they require high temperatures (>700 °C) for optimal performance (e.g., Ni-Ru/CeO2 achieves near-complete conversion at 700 °C [27]), leading to severe efficiency degradation below 400 °C.

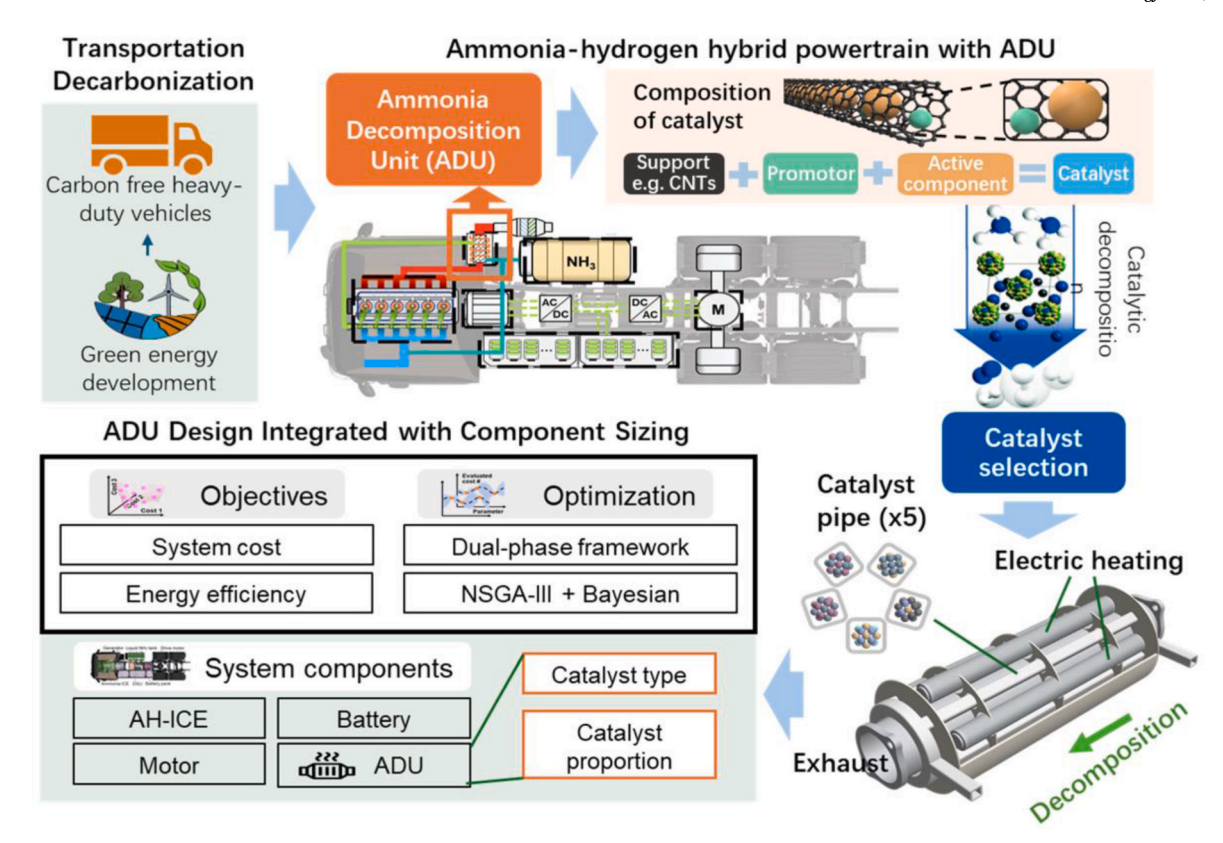


Fig. 1. Overall design of the research on surrogate-enhanced partitioned Pareto search for hydrogen production device optimization in carbon-free heavy-duty vehicles.



Fig. 2. Powertrain architectures of hybrid electric vehicle fueled with ammonia-hydrogen.

Moreover, the use of co-catalysts can further enhance the catalytic effect on certain catalysts. The design of active components, along with combinations of different supports and co-catalysts, gives rise to catalysts with distinct advantages. Existing ADU studies predominantly focus on catalyst selection while ignoring system-level integration. Furthermore, Zhang et al. analyzed the critical matching factor—ammonia decomposition rate—and proposed an ADU design framework incorporating waste heat recovery [13]. However, their approach prioritized catalytic efficiency over cost, creating efficiency-economic conflicts that necessitate further multi-objective optimization of catalysts and decomposers [29,30]. While these studies provide comprehensive multi-objective optimization frameworks, they fail to address the unique challenges of ammonia-hydrogen powertrains—a system whose component coupling relationships and complexity far exceed conventional hybrid vehicles. The catalytic system design requires tight coordination with other vehicle components, significantly impacting overall energy efficiency and stability. To the authors' knowledge, no existing studies address the co-optimization of hydrogen conversion rate, cost, and temperature through synergistic design of ammonia catalysts and other system components at the ammonia-hydrogen powertrain level, making this research critically significant.

Based on the aforementioned review and discussions, current research lacks a multi-objective optimization framework that balances system efficiency, catalytic performance, and cost under dynamic conditions, while neglecting the synergy between catalytic system design and powertrain component sizing. Through joint optimization with powertrain matching, catalytic systems can employ strategic catalyst combinations to achieve synergistic effects between macroscopic vehicle parameters and microscopic component characteristics. This paper proposes a surrogate-enhanced partitioned Pareto search for hydrogen production device optimization, which is shown in Fig. 1, which provides an effective methodology and demonstrates practical application of collaborative optimization of both the component sizing and the subsystem design for novel carbon-free heavy-duty vehicles. This study

 Table 1

 Catalyst specifications with values of main parameters.

No.	Catalyst (A-E/F/G-X/Y)	Temp (C)	GHSV (mL/ g _{cat} · h)	x (%)	L _{WR} (w/w %)
A	$Cs - Ru - \frac{MgO}{MII}$ [32]	400–500	15,000	84–100	5
В	$HEA - Co_{25}Mo_{45} - CNFs$ [33]	400–500	36,000	40–84	7.8
С	$\frac{CeO_2}{Al_2O_3} - CoCeAlO_x [34]$	400–500	30,000	10–65	100
D	LiNH ₂ [35]	400-500	7200	17-100	100
E	$CeO_2 - Ni [36]$	400-500	30,000	18-72.4	60
F	Ni – CeO ₂ [37]	400–500	13800 (Ar:NH3 = 1.3:1)	14–95	10
G	$Ru - CeO_2$ [37]	400–500	13800 (Ar:NH3 = 1.3:1)	77–100	2
H	Fe – BTC [38]	400-500	6000	9-73.8	34.7
I	$Ru - Al_2O_3$ [39]	400-500	18000	32-65	4.8
J	$\frac{Ni}{Ru}$ – CeO_2 [27]	400–500	15000	49.7–99.2	2.74

is featured with the following contributions: 1) A dual-phase optimization architecture combining genetic algorithm-based partitioned search with surrogate-guided refinement, co-designing component sizing and catalyst configurations for dynamic operating conditions to achieve efficient design of ammonia decomposition units in zero-carbon powertrains; 2) A surrogate-assisted convergence mechanism integrating adaptive domain partitioning and Bayesian optimization (BO) to prevent premature convergence in non-convex high-dimensional Pareto optimization, successfully coordinating powertrain parameters and catalyst composition variables through sequential domain decomposition and model-assisted merging; 3) A gradient-aware cooperative optimization protocol that systematically balances decomposition efficiency, material cost, and thermal adaptability through multi-catalyst synergy.

The remaining sections of this paper are structured as follows. Section 2 outlines data preparation and model establishment. Section 3 shows the optimization procedure of the ammonia-hydrogen hybrid system model. Section 4 presents and discusses the results of the model. Section 5 summarizes the key findings.

2. System modeling

This section outlines the key process descriptions and fundamental modeling assumptions that underpin the mathematical model developed for the on-board hydrogen production device and its integration within the heavy-duty vehicle powertrain, as shown in Fig. 2. This system integrates a detailed ADU model, the dynamics model, powertrain components model, alongside energy control systems. The powertrain, utilizing ammonia-hydrogen fuel, operates in pure electric, hybrid, and regenerative brake modes. The core assumptions made are as follows:

- It is assumed that hydrogen production from the ADU has no inertia, meaning the production rate instantaneously responds to changes in operating conditions. Consequently, fuel transport delays and associated losses are neglected for simplification of the system's dynamic response. Besides, the ADU conversion efficiency is primarily modeled as a function of two key parameters: operating temperature and catalyst activity. This captures the most significant factors influencing the decomposition process.
- The energy consumption of the ADU is quantified specifically as the total thermal energy required for both the endothermic ammonia decomposition reaction and the necessary preheating of the ammonia feed. Moreover, the ADU efficiency is precisely defined as the ratio of the energy content of the produced hydrogen to the

- energy content of the input ammonia, with careful consideration given to the energy consumed during the decomposition reaction.
- Overall system efficiency is calculated by considering the total energy input to the powertrain against the mechanical power output delivered for vehicle propulsion. Further, it is assumed that the thermal management system effectively utilizes and recovers waste heat from the engine exhaust to preheat the incoming ammonia feed before it enters the ADU, maximizing energy integration within the powertrain.

2.1. Catalyst selection and catalyst cost characterization

The ammonia-hydrogen hybrid system, primarily driven by the ADU, exhibits a high dependency on the judicious selection of catalysts within the ADU. In the ammonia decomposition reaction, the existing nitrogen-hydrogen bonds are broken, enabling the liberated hydrogen atoms to combine and form hydrogen gas. The process of breaking these nitrogen-hydrogen bonds necessitates either high temperatures or the presence of a catalyst to lower the activation energy. Catalysts facilitate this reaction by utilizing their active sites to attract hydrogen atoms, promoting their dissociation from nitrogen atoms and subsequent desorption, thereby allowing free hydrogen atoms to combine and form hydrogen gas. This decomposition mechanism can be expressed as follows [31]:

$$\begin{cases} NH_3(g) \rightarrow NH_3(aq) \\ NH_3(aq) \rightarrow NH_2(aq) + H(aq) \\ NH_2(aq) \rightarrow NH(aq) + H(aq) \\ NH(aq) \rightarrow N(aq) + H(aq) \\ 2N(aq) \rightarrow N_2(aq) \end{cases} \tag{1}$$

where (g) refers to the gas phase and (aq) refers to the adsorption of substances on the surface of the catalyst, rather than their original dissolution in water. At temperatures above 479 °C, the rate-limiting step for ammonia conversion is the cleavage of the N-H bond, which occurs in steps 1st~4th. Below this temperature, the limiting step shifts to nitrogen desorption, as seen in the 5th step.

The performance of these catalysts is reflected in various aspects, including catalyst stability, economic factors, catalytic efficiency, reaction rates, gas hourly space velocity (GHSV) and energy consumption. Table 1 lists the catalysts used in the catalytic model for this study.

Table 1 summarizes the ammonia conversion rates and catalyst preparation costs of various catalysts at low temperatures (400 °C, 450 °C, and 500 °C). The selected catalysts outperform others in terms of efficiency, cost, or a combination of both. Ru-Al2O3, Ru-CeO2, Fe-BTC, K-Ru-MgO/CNTs,Cs-Ru-MgO/MIL,Ni-CeO2 exhibit different catalytic effects depending on the support and co-catalysts used with the primary metal. Among these, Ru-Al2O3, Ru-CeO2, K-Ru-MgO/CNTs, Cs-Ru-MgO/ MIL are based on the most active precious metal, Ru. On the other hand, Fe-BTC and Ni- CeO2 use Fe and Ni, which are non-precious metals, with cost-effective supports such as BTC and CeO2 to maintain a strong catalytic activity at a lower cost. For example, Ni/Ru on CeO2 is a good representative of a low-temperature dual-metal catalyst, showing superior performance at a Ni:Ru molar ratio of 2.5:0.5, where ammonia conversion is approximately 10 % higher than at other ratios at 400 °C. In the case of multi-metal catalysts, CoMoFeNiCu high-entropy alloys (HEA) supported on celluouse nanofibers (CNFs) exhibit the best catalytic performance with a molar ratio of 25:45:10:10:10, as shown in the data from Joshua et al. Similarly, LiNH2 has been identified as a superior metal amide catalyst for ammonia decomposition, with LiNH2 showing higher conversion rates compared to NaNH2, as reported by Joshua W. This research includes LiNH2 and its data as a representative of metal amides, which have the advantage of higher structural controllability and simpler preparation processes due to the lack of a support or cocatalyst. The catalyst CeO2-Ni, based on a metal oxide catalyst where Ni serves as the support and CeO2 as the active component, showcases

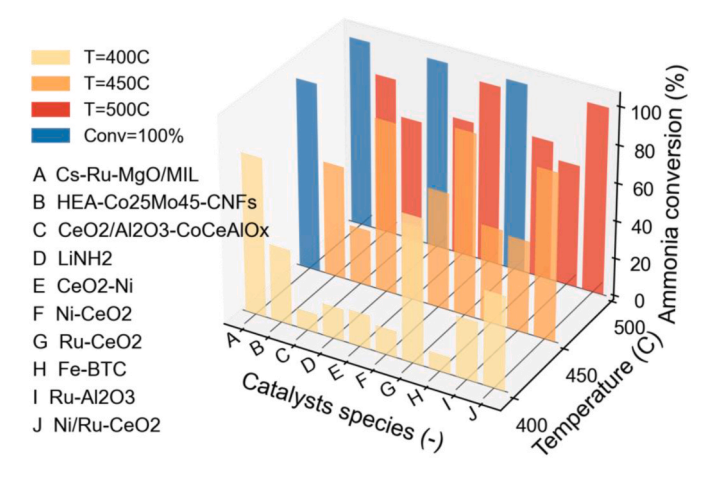


Fig. 3. Ammonia conversion rates of various catalysts at 400 $^{\circ}\text{C},\ 450$ $^{\circ}\text{C},\ and\ 500$ $^{\circ}\text{C}.$ The blue bars indicated the conversion of 100 percent.

the potential of metal oxide catalysts and suggests the possibility of reconsidering the relationship between the support and the active component. Graphic introductions for the relationship between ammonia conversion and temperature in the outlined catalysts are shown in Fig. 3.

The gas hourly space velocity GHSV defined in Eq. (2) is critical for understanding the relationship between ammonia flow rate and the catalyst volume:

$$GHSV = \frac{\dot{V}_{NH_3}}{V_{cat}} \tag{2}$$

where \dot{V}_{NH_3} is the ammonia volumetric flow rate (L·min⁻¹), and V_{cat} is the volume of the catalyst (L). In a catalytic system that uses the same ADU model, the GHSV is proportional to the ammonia flow rate. Nakisa's research on methane and ethylene shows that GHSV affects both conversion rates and selectivity, and that well-chosen GHSV results in the highest conversion rate under fixed other conditions [40]. In Table 1, the GHSV for each catalyst is set based on the conditions that maintain a balance between the hydrogen conversion rate and the hydrogen production rate. When multiple catalysts are used in combination, the GHSV must be optimized to maximize the ammonia conversion rate while maintaining the hydrogen production rate. This is predicted by the following formula:

$$v_f = \frac{\sum_{i=1}^{n} m_i \times v_i}{\sum_{i=1}^{n} W_i}$$
 (3)

where v_f is the predicted GHSV for the combination of catalysts that maximizes ammonia conversion, m_i is the mass fraction of the i th catalyst in the mixture, v_i is the highest GHSV of the i th catalyst for ammonia conversion, and W_i is the weight fraction of the i th catalyst.

The ammonia conversion rate is defined differently in various studies. For instance, Xie et al. defined the ammonia conversion rate as [33]:

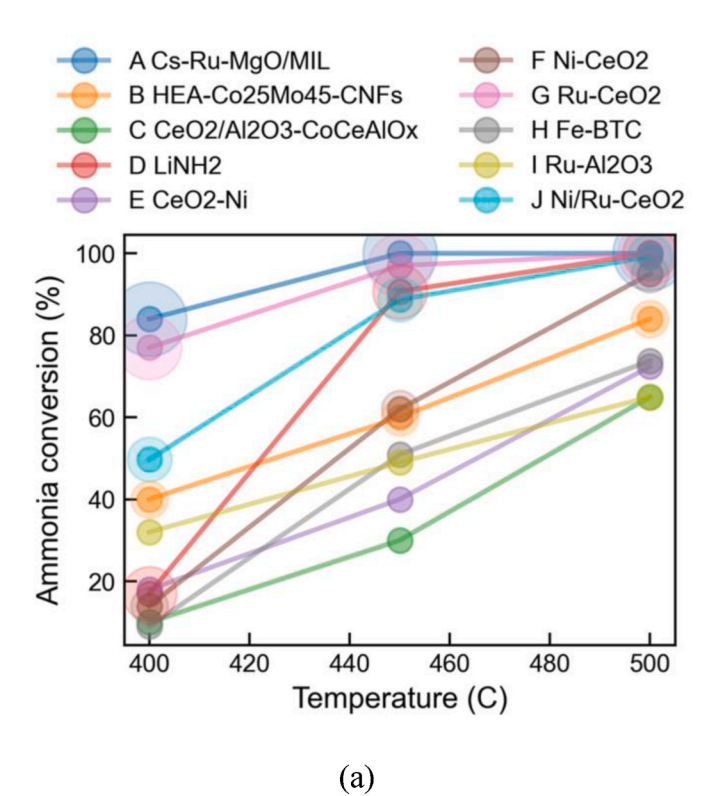
$$x = \frac{F_{inNH_3} - F_{outNH_3}}{F_{inNH_3}} \times 100\%$$
 (4)

where F_{inNH_3} and F_{outNH_3} are the molar flow rates of ammonia entering and exiting the reactor, in mol NH_3/s .

On the other hand, Ilaria et al. used the following formula for the ammonia conversion rate [38]:

$$x = \frac{[NH_3]_{in} - [NH_3]_{out}}{(1 + [NH_3]_{out}) \times [NH_3]_{in}} \times 100\%$$
 (5)

where $[NH_3]_{in}$ and $[NH_3]_{out}$ are the concentrations of ammonia at the



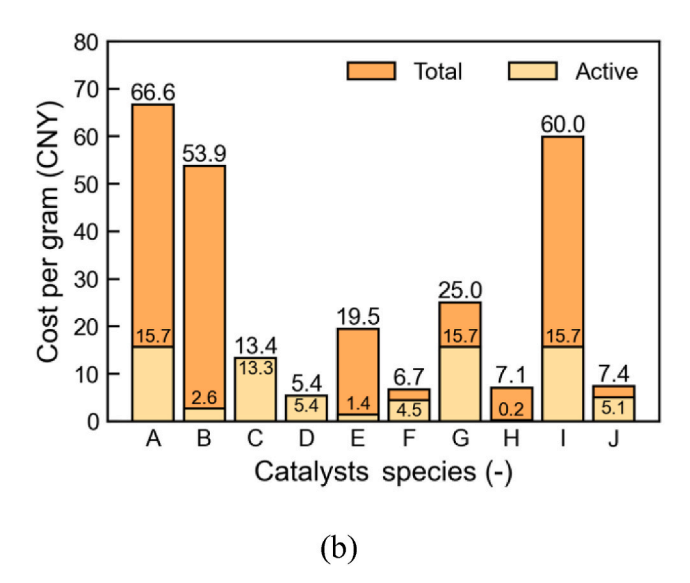


Fig. 4. Visualization of tabular data: (a) Comparison of catalyst conversion rate under different temperatures with ammonia conversion $>\!80$ % at 450C and 500C emphasized; (b) Total cost in RMB per gram of catalyst across various kinds of catalysts, where the yellow regions represent costs of active components.

reactor inlet and outlet, respectively.

There are slight differences in measurement methods between these definitions, such as the use of a Poropak Q column and gas chromatography-barrier ionization detector (GC-BID) for measuring hydrogen input and output concentrations in Xie et al.'s study, which is not detailed in Ilaria et al.'s study. However, as observed in the study by Yin et al., in the $400-450~^{\circ}\text{C}$ range, temperature is the primary factor influencing ammonia conversion, while reaction time has little effect. Therefore, the differences due to measurement intervals can be considered negligible. Fig. 4 shows the specific influence of each catalyst on ammonia conversion at different temperatures and the cost factors.

Table 2
Costs of catalyst with components.

No.	Catalysts (A- E/F/G-X/Y)	W _{act} (w/w %)	P _{sup} (CNY/ g)	W _{sup} (w/w %)	Cost P _{act} (CNY/g)	$\begin{array}{c} \text{Cost } P_{tot} \\ (\text{CNY}/\\ g_{cat}) \end{array}$
A	$Cs - Ru - \frac{MgO}{MIL}$	1.38 ($W_{pro} = 3.62$)	9.07	95	1134.83 ($P_{pro} = 1137.8$)	66.63
В	HEA – Co ₂₅ Mo ₄₅ – CNFs	7.8	55.54	92.2	33.92	53.85
С	$rac{CeO_2}{Al_2O_3}- \ CoCeAlO_x$	100	-	0	13.36	13.36
D	$LiNH_2$	100	_	0	5.44	5.44
E	$CeO_2 - Ni$	60	45.13	40	2.39	19.49
F	$Ni-CeO_2$	10	2.39	90	45.13	6.66
G	$Ru-CeO_2$	2	2.39	98	1134.83	25.04
H	Fe-BTC	34.7	10.55	65.3	0.57	7.09
I	$Ru - Al_2O_3$	4.8	5.78	95.2	1134.83	59.97
J	$\frac{Ni}{Ru}$ – CeO_2	2.8	2.39	97.2	180.6	7.38

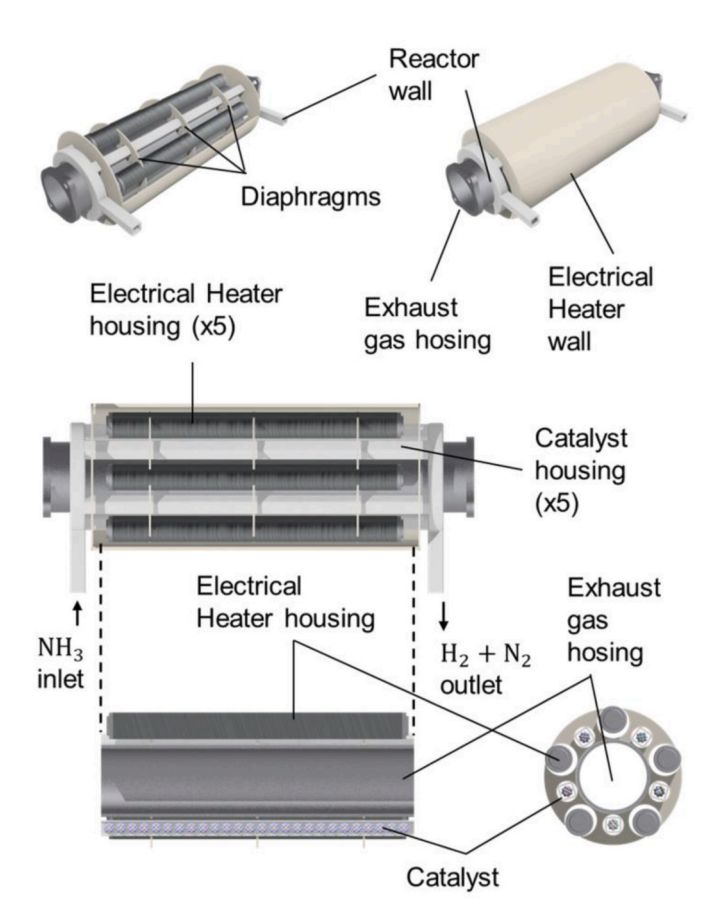


Fig. 5. Schematic diagram of the internal structure of the ADU

The determinants of the cost metric encompass the unit raw material cost of individual catalysts, the total cost of composite catalysts derived from the calculated amounts of each catalyst component, and the manufacturing costs of other powertrain components. Since the reactor setup for composite catalysts remains consistent irrespective of the selected catalyst type, its cost indicator does not influence the comparative evaluation among different catalysts. The total cost of a composite catalyst is calculated based on the quantity and cost indicator of each constituent catalyst. Regarding the unit cost of individual catalysts, direct data is not always available for some, necessitating their calcu-

lation. The calculation of the catalyst cost per gram is as follows

$$P_{tot} = P_{pro} \times W_{pro} + P_{act} \times W_{act} + P_{sup} \times W_{sup}$$
 (6)

where P_{pro} , P_{act} , P_{sup} represent the cost per gram of the promoter, active component, and support material, respectively, and W_{pro} , W_{act} , W_{sup} represent the mass fractions of the promoter, active component, and support material in the catalyst. The reference cost indicator of LiNH2 is obtained from Thomas Scientific, and the cost indicator of other materials are sourced from Sigma Aldrich. Data are retrieved using reagent-grade materials at the maximum purchase specification cost per gram. The cost calculations are summarized in Table 2.

For the catalysts K-Ru-MgO/CNTs, Cs-Ru-MgO/MIL, and HEA-Co25Mo45-CNFs, which are synthesized by the researchers, the cost calculation is based on the materials used in their preparation, with the component costs calculated according to their proportions. The material costs are referenced from Sigma Aldrich. For the MgO/CNT support of K-Ru-MgO/CNTs, the MgO/MIL support of Cs-Ru-MgO/MIL, the HEA support, and the CeO2/Al2O3-CoCeAlOx support and promoter, since the specific components cannot be directly purchased, the catalyst preparation cost is calculated using the raw materials specified in the synthesis methods, considering the molar ratios of each component.

For promoters, active components, or supports composed of more than one material, the cost per gram is calculated based on the materials used and their respective mass fractions in the preparation. The mass fractions are converted from the given molar ratios. The conversion of mass fractions and the calculation of the cost for the active component are described as follows:

$$\begin{cases} W_i = \frac{M_i \times n_i}{\sum_{i=1}^N M_i \times n_i} \\ P_{act} = \sum_{i=1}^N P_i \times W_i \end{cases}$$
 (7)

where M_i is the molar mass of the i-th element in the active component, n_i is the number of moles of the i-th element in 1 mol of the active component, P_i is the cost per gram of the material corresponding to the i-th element, and W_i is the mass fraction of the i-th element in the active component.

2.2. Application of ammonia decomposition catalysts in hybrid power systems

2.2.1. Structure of ADU

The ADU consists of the engine exhaust outlet pipe, a catalytic unit where ammonia passes through the catalyst, and an external heating layer. In the ammonia-hydrogen hybrid system, the exhaust gas temperature of the engine is approximately 400 $^{\circ}$ C, while the temperature required for low-temperature catalysis may reach up to 500 $^{\circ}$ C. Therefore, in addition to heating the exhaust gases, a supplementary heating layer is necessary to achieve the appropriate catalytic temperature. The structure of the ADU plays a crucial role in heating efficiency. It must ensure that the catalyst tube, exhaust pipe and heater are in sufficient contact to minimize heat loss during the heat transfer process, as illustrated in Fig. 5.

The heating layer utilizes electric heating, and working in conjunction with the exhaust gases, it helps conserve the energy consumption of the electric heating layer. The catalyst pipeline is divided into five individual pipes from the main exhaust pipe, with the catalyst evenly distributed throughout each catalytic tube. These catalytic tubes alternately wrap by electric heaters along the exhaust pipe. Ammonia, introduced from the ammonia storage tank, is catalytically decomposed into hydrogen in the ADU, and then mixes with the ammonia that flows directly out of the ammonia storage tank before being injected into the injector. After combustion, the exhaust gases flow into the exhaust pipe, where they again undergo energy conversion to provide the necessary

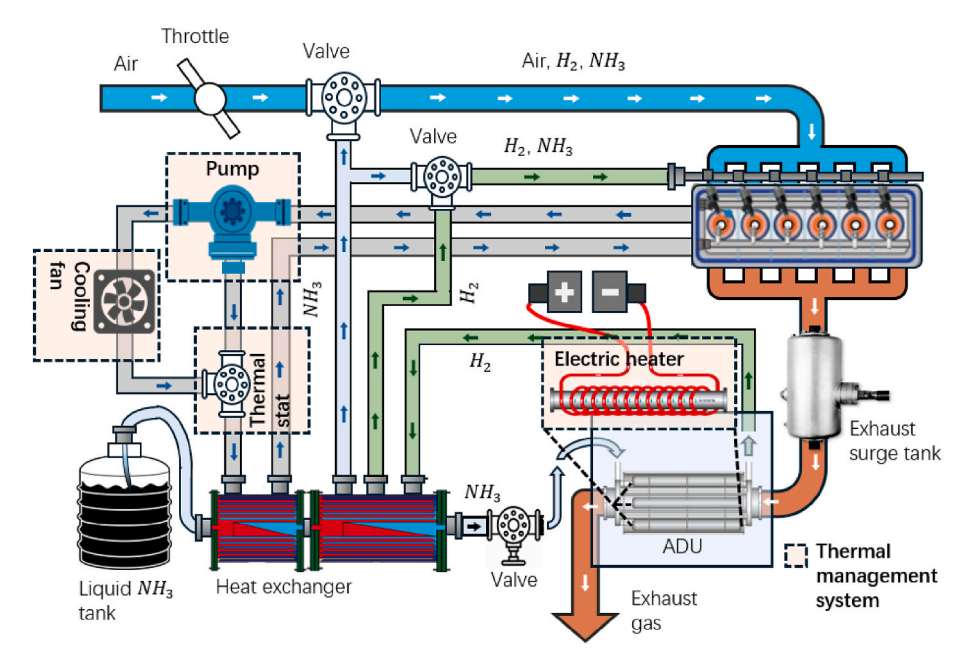


Fig. 6. Schematic diagram of the carbon-free hybrid electric powertrain fueled with ammonia and hydrogen, first proposed in the Chinese Patent NO. ZL202111460076.9 by Wang and Zhang et al. [6].

heat for the subsequent ammonia decomposition process.

The division of the catalytic pipes within the ADU not only increases the heat efficiency of catalytic tubes but also allows various types of catalysts with different properties to be physically combined, granting the ADU new characteristics. By independently controlling the flow rate, temperature, and pressure of each pipe, the ADU can precisely adjust the reaction environment for each catalyst, ensuring that the catalytic environment in each tube closely matches the conditions under which the catalysts exhibit their optimal catalytic efficiency in the laboratory. The types of catalysts and their respective proportions within each pipe have a significant impact on the ammonia conversion rate and overall system cost. These effects are governed by the following formulas:

$$\begin{cases} x_{tot}^{ADU} = \sum_{i=1}^{n} x_{i}^{ADU} \cdot W_{i}^{ADU} \\ Price_{tot}^{ADU} = m_{tot}^{ADU} \cdot \sum_{i=1}^{n} \left(Price_{i}^{ADU} \cdot W_{i}^{ADU} \right) \end{cases}$$
(8)

where x_i^{ADU} is the ammonia conversion rate of the catalyst in the *i*-th catalytic tube, W_i^{ADU} is the mass ratio of the catalyst in the *i*-th catalytic tube, m_{tot}^{ADU} is the total mass of the catalysts across all catalytic tubes in the ADU, and $Price_i^{ADU}$ is the cost per gram of the catalyst in the *i*-th catalytic tube.

2.2.2. Thermal energy management system

In the heating process of the ADU, the engine coolant preheats the catalyst within the ADU, whereas the engine exhaust waste heat and electric heaters further heat the ammonia flow within the catalytic pipes to the required catalytic temperature. The model simulates the efficiency, cost, and operating conditions of different catalyst combinations. The efficiency of the system is determined by the energy required for physical and chemical heating, the hydrogen consumption rate, and the ammonia conversion rate. The energy required for physical and chemical heating is calculated by the following formulas:

$$\begin{cases}
Q_{physical} = C_{steel} \times \frac{m_{ADU}}{1000} \times \Delta T \\
Q_{chemical} = \Delta H \times m_{H_2}
\end{cases}$$
(9)

where $Q_{physical}$ represents the energy required for physical heating of the ADU, ΔT is the temperature change required for physical heating, and C_{steel} is the specific heat capacity of the steel used in the catalytic pipe. $Q_{chemical}$ represents the energy required for the chemical reaction to convert ammonia into hydrogen, where ΔH is the enthalpy change and m_{H_2} is the mass of hydrogen produced. Thus, the total energy required to heat the ADU can be expressed as

$$P_{ADU} = Q_{physical} + Q_{chemical} \tag{10}$$

The efficiency of the ADU system, based on energy consumption, is calculated as follows:

$$Eff_{ADU} = \frac{m_{H_2} \times LHV_{H_2}}{m_{NH_3} \times LHV_{NH_3} + P_{ADU}}$$

$$\tag{11}$$

where LHV_{H_2} is the lower heating value (LHV) of hydrogen, representing the heat released during hydrogen combustion, and LHV_{NH_3} is the LHV of ammonia.

In the energy conversion process of the ammonia-hydrogen engine, combustion of ammonia and hydrogen converts chemical energy into mechanical energy to drive the crankshaft, which is further converted by the generator into electrical energy for battery charging, vehicle propulsion, and heating the ADU. The combustion reactions for ammonia and hydrogen in the engine are:

$$\begin{cases} NH_3 + 0.75(O_2 + 3.76N_2) \rightarrow 1.5H_2O + 3.32N_2 \\ H_2 + 0.5(O_2 + 3.76N_2) \rightarrow H_2O + 1.88N_2 \end{cases}$$
(12)

The LHV of the mixed fuel is calculated as:

$$\begin{cases} LHV_{mix} = \frac{LHV_{NH_3} + a_{mix}^m \cdot LHV_{H_2}}{1 + a_{mix}^m} \\ a_{mix}^m = a_{mix}^v \cdot \frac{\rho_{H_2}}{\rho_{NH_2}} \end{cases}$$

$$(13)$$

The engine waste heat, engine power, heat generated during combustion, and heat removed by exhaust are governed by the energy conservation equation:

$$m_{ICE}c_{ICE}\frac{dT_{ICE}^{cool}}{dt} = E_{ICE}^{rea} - P_{ICE} - Q_{ICE}^{exh}$$

$$\tag{14}$$

Thus, the heat that still needs to be supplied by the electric heater,

Table 3 Vehicle technical specifications.

Vehicle parameters	Value and unit	
Gross weight mgw	49,000 kg	
Wheel radius r	0.512m	
Rolling resistance f	0.012	
Air resistance coefficient C_D	0.65	
Frontal area A_f	9.45m ²	
Gravitational acceleration g	$9.80 \ m \cdot s^{-2}$	
Transmission mechanical efficiency η_t	0.94	
Fianl drive ratio i_0	4.3	
AMT gear ratio $i_{\rm g}$	15.53/12.8/9.39/7.33/5.73/4.46/3.48/2.71/ 2.1/1.64/1.28/1	

considering the waste heat from the engine, is expressed by:

$$Q_{Elec} = P_{ADU} - Q_{ICE}^{exh} = \left(C_{steel} \times \frac{m_{ADU}}{1000} \times \Delta T + \Delta H \times m_{H_2}\right)$$
$$-\left(E_{ICE}^{rea} - P_{ICE} - m_{ICE}c_{ICE}\frac{dT_{ICE}^{rool}}{dt}\right)$$
(15)

2.2.3. Ammonia-hydrogen hybrid powertrain system model

The catalyst optimization model developed in this paper focuses on its application in the driving environment of electric heavy-duty commercial trucks. The ammonia-hydrogen fuel, in cooperation with the electric motor, develops operation modes for the power system, including: pure electric mode, engine hybrid mode, and braking recovery. In pure electric mode, the power required for vehicle operation is entirely supplied by the generator, while the generator also provides electric heating for the ADU to supply the heat necessary for ammonia decomposition, allowing the vehicle to switch to the engine hybrid mode that combines ammonia-hydrogen fuel with the battery at any time. The schematic of the zero-carbon hybrid powertrain of the electric vehicle is shown in Fig. 6. Moreover, vehicle technical parameters are shown in

Table 3,where m_{gw} refers to the gross weight of vehicle, g refers to the local gravitational acceleration, f refers to the rolling resistance, C_D refers to the air resistance coefficient and A_f refers to the vehicle frontal area. r and i denote the wheel radius and the main reducer speed ratio, respectively. α is road slope, ρ is air density, and ν is velocity. δ refers to the conversion coefficient of the rotating mass.

Table 4
Mass of vehicle components.

Parameters	Value and units
Engine mass J_2^{ICE}	$1.18P_{ICE}^{max}$ kg
Generator mass J_2^{GEN}	$1.32P_{GEN}^{max}$ kg
Motor mass J_2^{DM}	$1.32P_{DM}^{max}$ kg
Battery mass J_2^{bat}	$13.6Q_{bat}$ kg

Table 5Definition of the multi-objective optimization problem.

Parameter	Definition
Objective functions	$\min[f_1,f_2]$
Driving cycle	Standard driving cycle
Variables to be optimized	$150 \text{ kW} \le P_{ICE}^{max} \le 300 \text{ kW}$
	$350 \text{ kW} \le P_{DM}^{max} \le 550 \text{ kW}$
	$10 \text{ kWh} \leq E_{bat} \leq 40 \text{ kWh}$
	$ ho_i^{cat} \in [A \sim J], \ i = I, II, III, IV, V$
	$0 \le \rho_i^{cat} \le 1, i = I, II, III, IV, V$
Constraints	$ ho_{ ext{I}}^{cat}+ ho_{ ext{II}}^{cat}+ ho_{ ext{III}}^{cat}+ ho_{ ext{IV}}^{cat}+ ho_{ ext{V}}^{cat}=1$
	$P_{GEN}^{max} = P_{ICE}^{max}$
	$P_{ICE}^{min} \leq P_{ICE} \leq P_{ICE}^{max}$
	$P_{GEN}^{min} \leq P_{GEN} \leq P_{GEN}^{max}$
	$P_{DM}^{min} \leq P_{DM} \leq P_{DM}^{max}$
	$P_{bat}^{min} \leq P_{bat} \leq P_{bat}^{max}$
	$SOC_{min} \leq SOC \leq SOC_{max}$

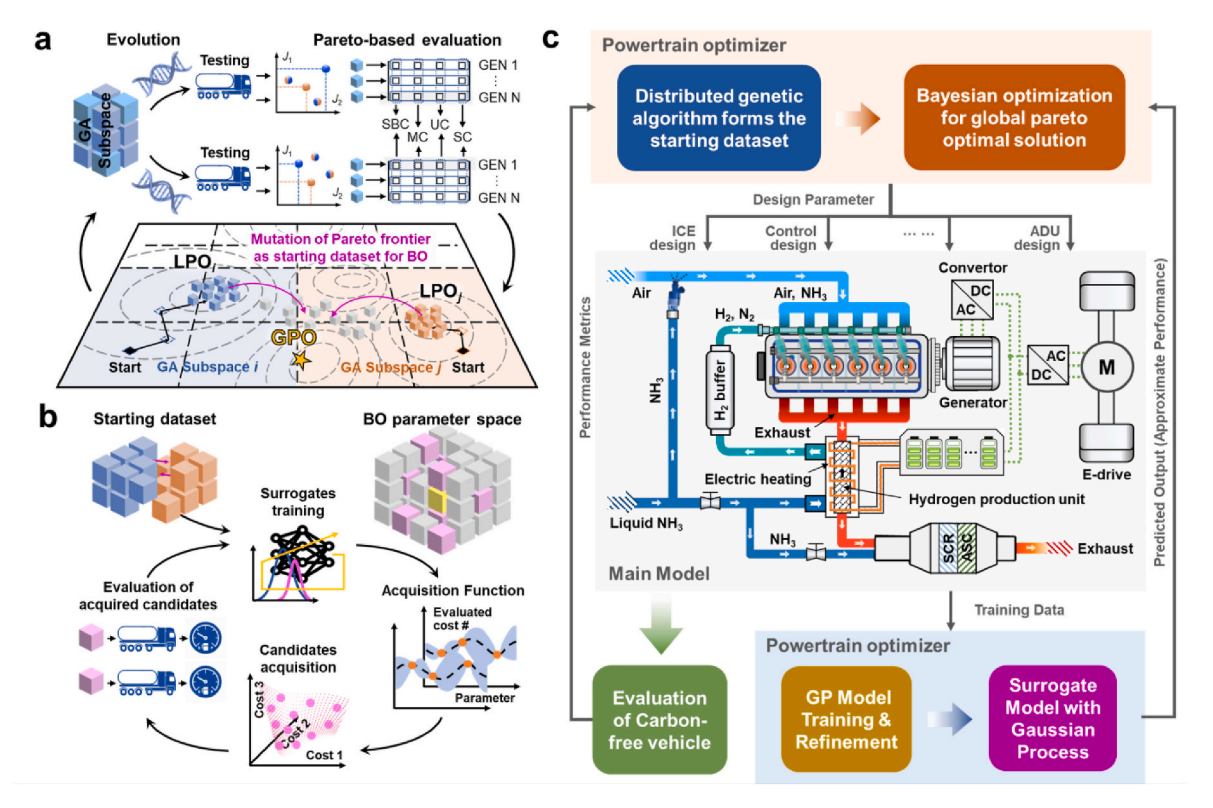


Fig. 7. Schematic diagram of surrogate-enhanced partitioned optimization for carbon-free heavy-duty vehicles: (a) Partitioned NSGA-III optimization with surrogate co-training: Global exploration phase, including a crossover pool; (b) Cross-region surrogate transfer and Bayesian refinement: Local exploitation phase; (c) Methodology flowchart: Overall framework for ADU design and powertrain optimization.. (Full definitions of abbreviations can be found in the main text.)

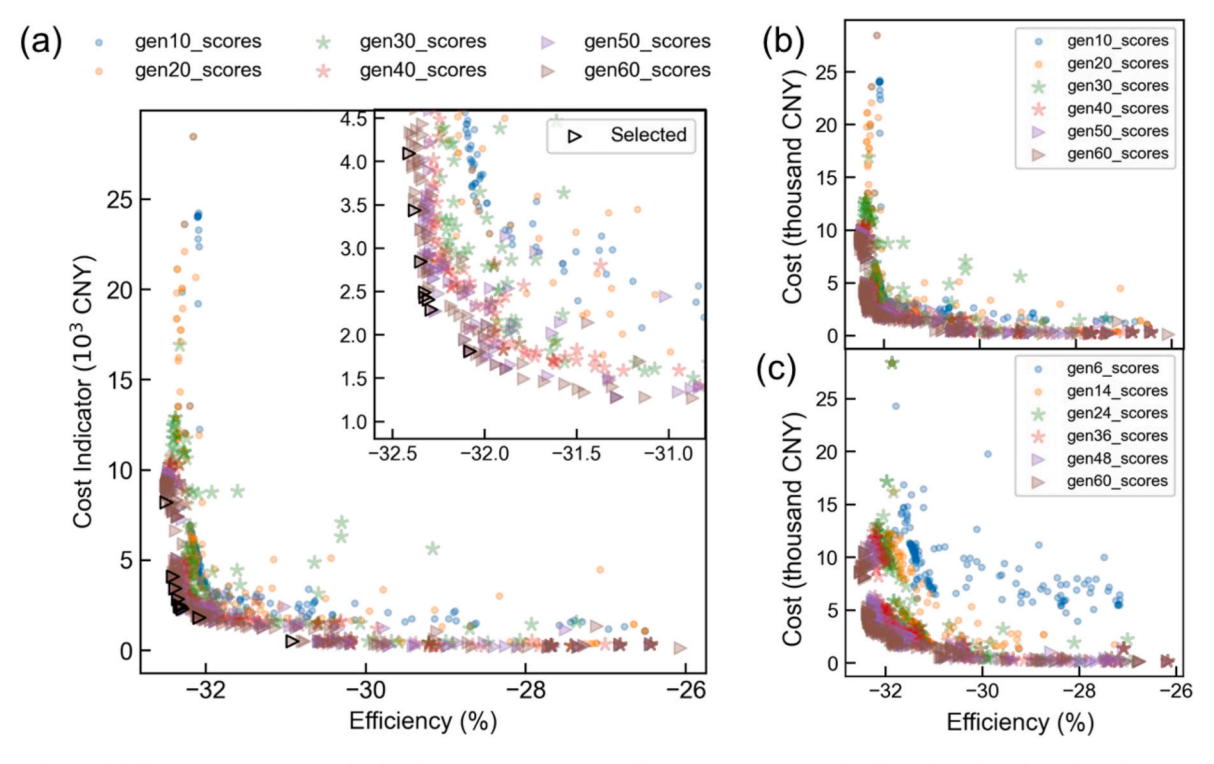


Fig. 8. Pareto fronts of different generations. (a) The distribution variation of cost-efficiency optimization of 10th, 20th, 30th, 40th, 50th, 60th generation and the magnified display for the best combinations at upper right corner, where the black triangle icons refer to the selected Pareto optimal solutions. (b) and (c) are the comparison between two sets of generation variations, where (b) is for 10th, 20th, 30th, 40th, 50th, 60th generation and (c) is for 6th, 14th, 24th, 36th, 48th, 60th generation.

Table 6Trade-off solutions of the best stretegy in the 60th generation.

Parameters	Trade-off (60th)	
P _{ICE} ^{max} (kW)	307.26	
P_{DM}^{max} (kW)	432.48	
E_{bat} (kWh)	63.49	
ρ_i^{cat} type vector (–)	[D,E,E,E,G]	
ρ_i^{cat} proportion vector (%)	[20.34,19.70,19.71,19.71,20.54]	

In the model, the power demand P_{dem} for the vehicle under full load and the power supplied by the generator P_{DM} are calculated using the following equations:

$$\begin{cases} P_{dem} = (P_{ICE}\eta_{GEN} + P_{bat} - P_{aux})\eta_{DM}\eta_f \\ P_{DM} = k_p^{\alpha}(\nu_{ref} - \nu) + k_p^{\alpha} \int_0^t (\nu_{ref} - \nu)dt \end{cases}$$
(16)

where P_{bat} and P_{aux} refer to the power of battery and auxiliary devices, respectively. η_{DM} and η_f denote the efficiency of drive motor and final

drive respectively.

The power from the generator that is used to drive the electric heater to heat the ADU is denoted by $\frac{dQ_{Ele}}{dt}$, with the remainder used for vehicle propulsion power, P_{ele}^{dri} . Therefore, the power supplied by the generator to drive the vehicle P_{ele}^{dri} , the power provided by the combustion of mixed fuel in the engine to propel the vehicle P_{ICE} and the total power P_{tot}^{dri} provided by the ammonia-hydrogen hybrid system are calculated by the following formulas:

$$\begin{cases}
P_{ele}^{dri} = P_{DM} - \frac{dQ_{Ele}}{dt} \\
P_{ICE} = \frac{\omega_{ICE} T_{ICE}}{9550} \\
P_{tot}^{dri} = P_{ele}^{dri} + P_{ICE}
\end{cases}$$
(17)

In pure electric mode, the vehicle's power is entirely supplied by the generator. Part of the generator's power is used to heat the ADU, while most of the power is used to propel the vehicle. In hybrid engine mode, vehicle power is supplied jointly by the engine and the generator, and some of the generator power is used to maintain the temperature of the

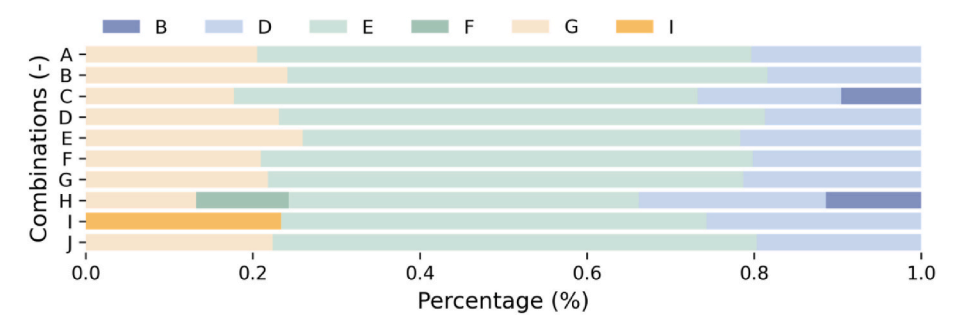


Fig. 9. Gradients of the 10 selected combinations.

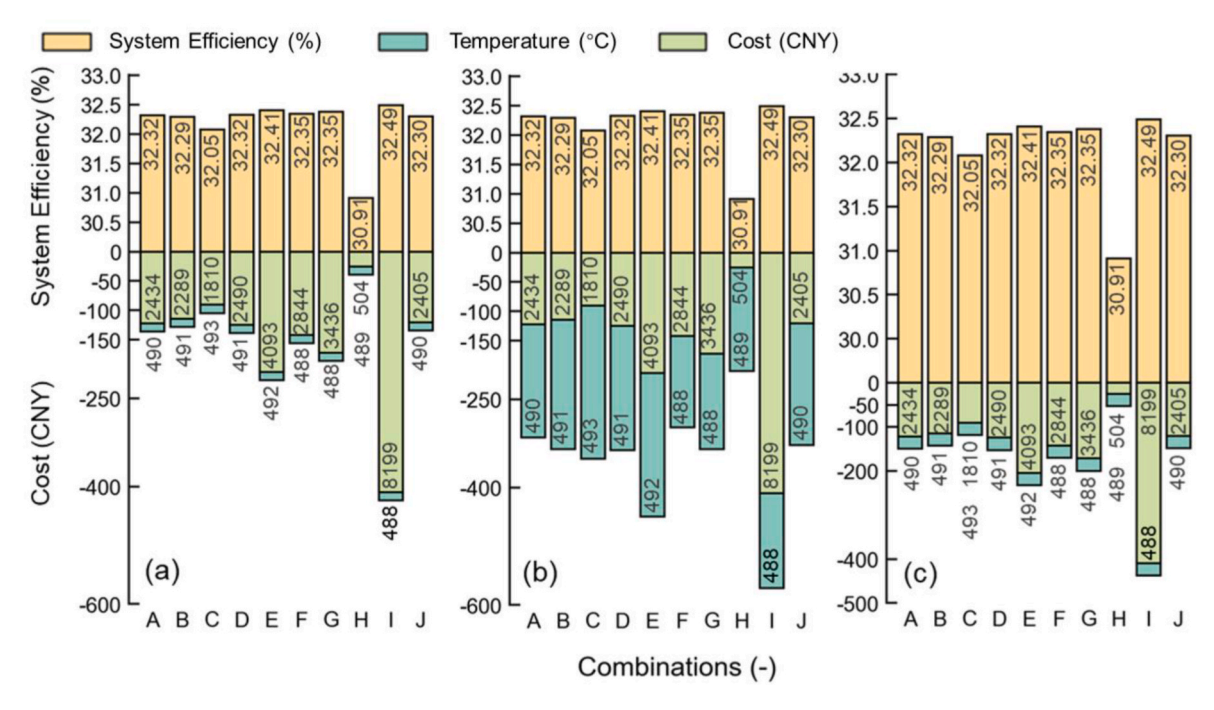


Fig. 10. Performance of the selected 10 combinations which are the closest to the Pareto surface is demonstrated with different focus as which (a) focus on the effect of the costs, (b) focus on the effect of the temperatures, and (c) focus on the effect of the system efficiency.

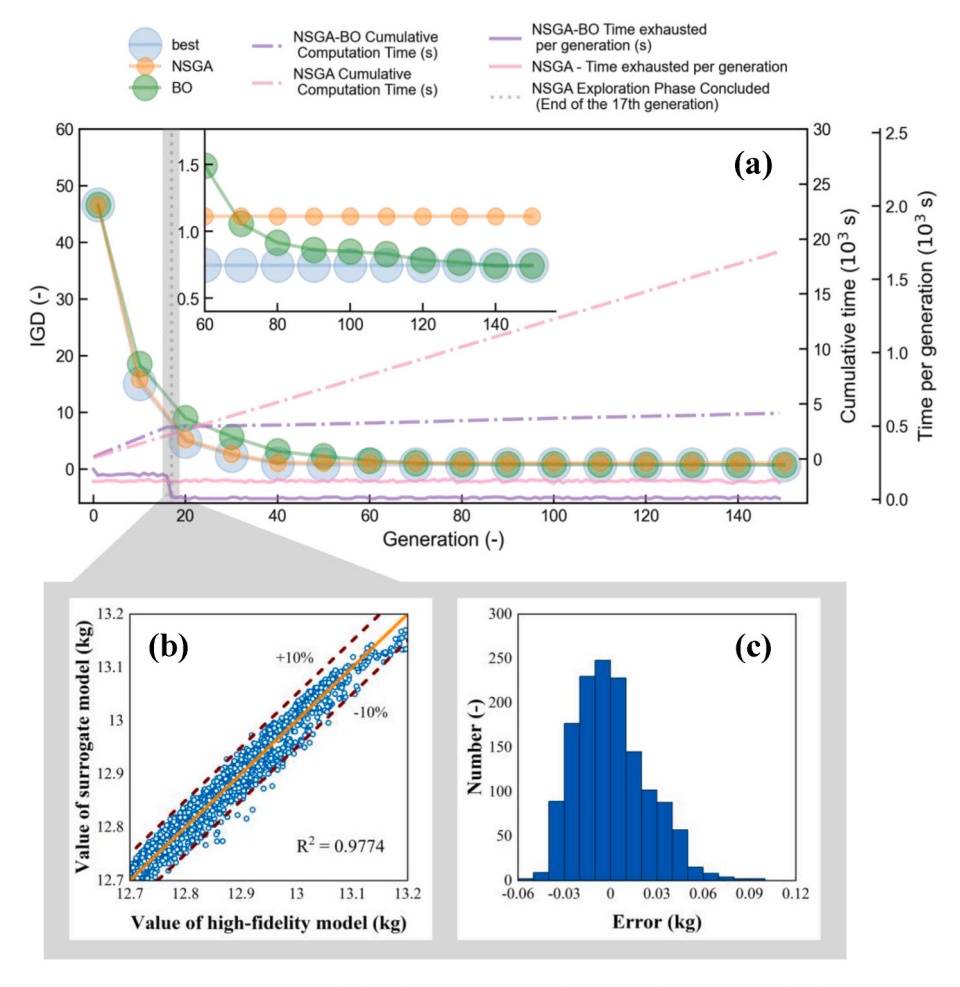
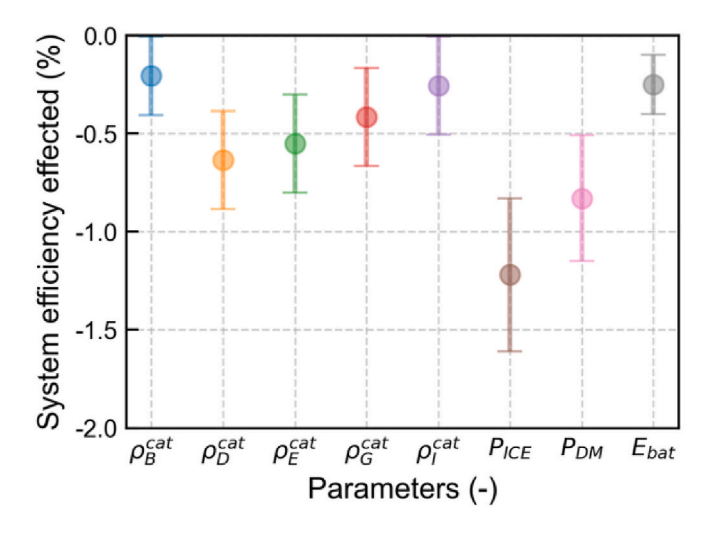
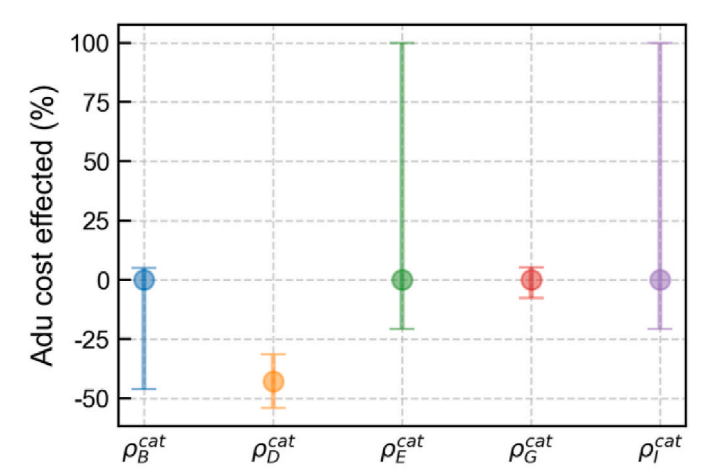


Fig. 11. Comparison of algorithms in merging efficiency and computation load.





(a)

Fig. 12. Sensitivity analysis for system efficiency (a) and ADU cost (b).

Parameters (-)

(b)

 ρ_G^{cat}

ADU.

3. Surrogate-enhanced multi-objective optimization of

 ho_D^{cat}

 ρ_B^{cat}

This paper proposes a dual-phase optimization framework that combines partitioned NSGA-III exploration with BO refinement. The feasible region is first divided into subregions, each optimized independently using NSGA-III to generate local Pareto fronts and training data for surrogate models. Adjacent subregions with boundary solution clustering are then merged, and BO refines the combined Pareto front using Gaussian process (GP) surrogates. The process iterates until convergence, achieving a globally optimal Pareto set while balancing exploration and exploitation. This approach effectively addresses highdimensional, nonconvex optimization challenges in ammoniahydrogen hybrid powertrain design.

The use of surrogate model is essential in the optimization process. While the mathematical model simplifies key interactions, it remains too computationally intensive for full multi-objective optimization. GP, as the core of BO, offers theoretical strengths for continuously validating its role as an surrogate model for costly physical models. GP defines a

function distribution via mean and covariance, and is updated using Bayesian inference when new high-fidelity data is available. This yields both predictive means and variances, quantifying uncertainty. Through hyperparameter tuning, the covariance captures system patterns, while BO's acquisition function leverages both predictions to strategically sample regions with high uncertainty or potential gain. This focused data acquisition reduces uncertainty where optimal solutions are likely, allowing GP to self-validate dynamically. As predictive uncertainty drops and GP predictions converge with physical model outputs, the surrogate model's fidelity and optimization guidance are confirmed—ensuring the Pareto front achieves both theoretical optimality and engineering feasibility.

3.1. Problem formation

In this work, the objective functions for component sizing optimization are defined as system energy efficiency (f_1) and system cost (f_2) . Let $x \in \mathbb{R}^N$ denotes the decision variables of the system under optimization, and let $F(x) = [f_1(x), ..., f_K(x)]$ represents the vector of K = 2conflicting objective functions to be minimized. The optimization problem is formalized as follows, where $S \subset \mathbb{R}^N$ represents the feasible

$$\min F(x) = [f_1(x), \dots, f_K(x)], \text{ subject to } x \in S,$$
(18)

The goal is to identify the Pareto-optimal set X^* , such that no objective function can be improved without worsening at least one other objective. A solution $x^* \in S$ is Pareto-optimal if:

$$\nexists x \in S : F(x) \prec F(x^*), \tag{19}$$

where $F(x) \prec F(x^*)$ implies F(x) dominates $F(x^*)$ in all objectives. For two solutions x_1 and x_2 , x_1 dominates x_2 if:

$$f_i(x_1) \le f_i(x_1) \quad \forall i = 1, 2, ..., K \quad and \quad \exists j : f_i(x_1) < f_i(x_1).$$
 (20)

Given the high-dimensional nature of the decision space and the nonconvexity of the objectives, direct global search can be computationally expensive. To overcome this, we propose a dual-phase optimization approach for the design of the ADU for ammonia-hydrogen hybrid vehicle, which is depicted as shown in Fig. 7. In this figure, the main model detailed in Section 2 functions as a high-fidelity physical representation of the powertrain. This model serves as the external evaluation environment, interacting iteratively with the optimizer. The surrogate-enhanced optimizer proposes a set of design and control parameters for the physical model's components in each iteration. The main model then executes a comprehensive simulation run under these assigned parameters, typically across various driving cycles, and outputs the resulting vehicle performance metrics to the optimizer. Initially, the global exploration phase, depicted in Fig. 7 (a), employs a partitioned NSGA-III to systematically explore the design space. Within this phase, population diversity and exploration are enhanced through a crossover pool that utilizes four distinct operators: simulation binary crossover (SBC), shuffle crossover (SC), multi-point crossover (MC), and uniform crossover (UC). Promising solutions identified during this exploration, forming local Pareto Optimal (LPO) frontiers, are then transferred to the subsequent refinement stage. Fig. 7 (b) outlines the local exploitation phase, where Bayesian optimization refines these solutions. Gaussian Process surrogate models are trained using the collected data, and an acquisition function intelligently guides the search for new, highly beneficial design points. This iterative process drives the optimization towards global Pareto optimal (GPO) from the local Pareto optimal (LPO). Finally, Fig. 7 (c) presents the overarching methodology flowchart, integrating the ADU design and component sizing within the powertrain configuration. This holistic view demonstrates how the genetic exploration and Bayesian refinement work in synergy to enable a dynamic evaluation of the ammonia-hydrogen heavy-duty vehicle.

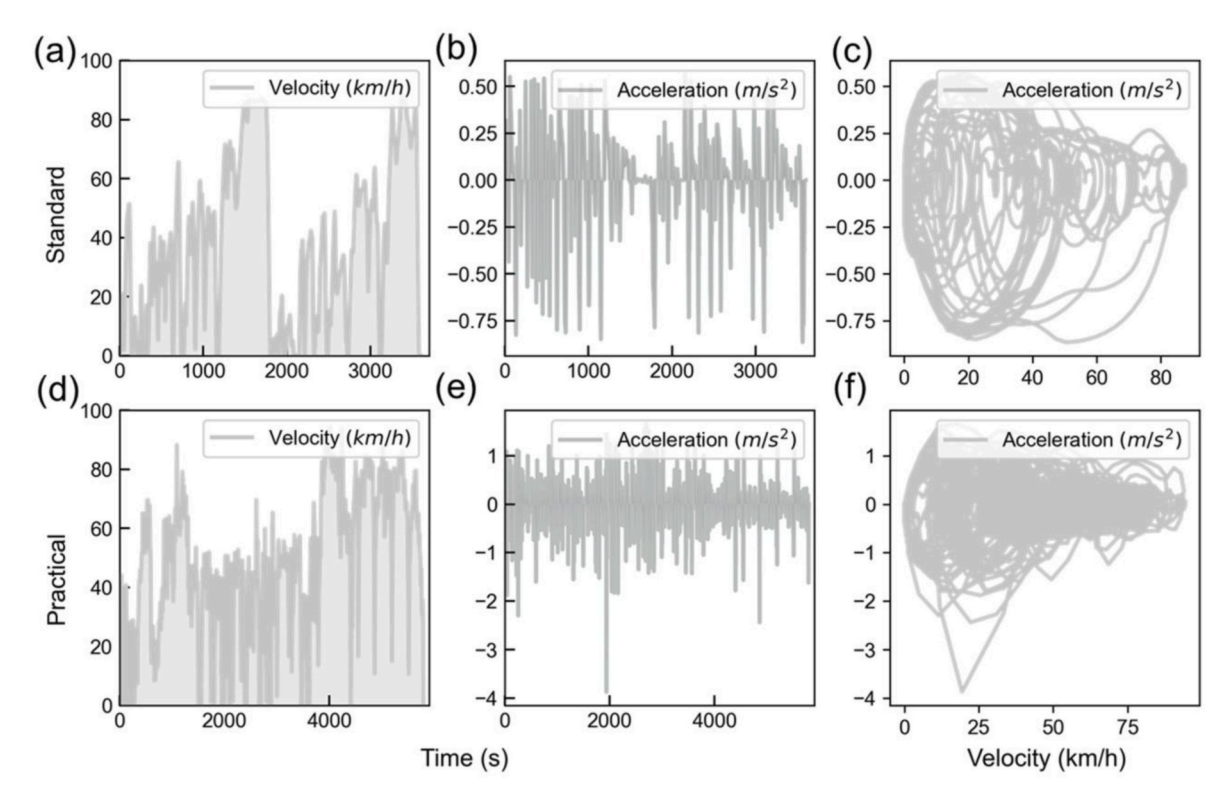


Fig. 13. (a) The standard driving cycle combining CHTC and CWTVC driving cycle. (b) Acceleration variation of standard driving cycle. (c) Acceleration against velocity of standard driving cycle. (d) The practical driving cycle combining three situations of RD driving cycles. (e) Acceleration variation of practical driving cycle. (f) Acceleration against velocity of practical driving cycle.

3.2. Partitioned NSGA-III optimization with surrogate preparation

The optimization framework shown in Fig. 7 establishes a synergistic relationship between a high-fidelity physical model, a hybrid NSGA-III/BO optimizer, and a Gaussian process surrogate model. The core process is as follows: the optimizer generates candidate solutions, which are then accurately evaluated by the computationally expensive physical model. These evaluation results are used to train the surrogate model.

The surrogate model's key role is to provide rapid performance estimates, which guide the optimization search efficiently while significantly reducing computational costs. This closed-loop interaction ensures that while the search is guided by the fast surrogate, all critical solutions are validated by the accurate physical model, guaranteeing the final results are implementable. This creates a self-reinforcing cycle: evaluation data from the physical model continuously improves the surrogate's accuracy, and a more accurate surrogate, in turn, enables a more effective search by the optimizer.

The partitioned optimization process integrates data generation for surrogate modeling as an intrinsic component of the NSGA-III evolution. To enable efficient search, we partition the feasible region $S \subset \mathbb{R}^N$ into i non-overlapping subregions S_1, S_2, \ldots, S_i such that:

$$\begin{cases}
S = \bigcup_{j=1}^{i} S_{j}, S_{j} \cap S_{k} = \emptyset \forall_{j} \neq k, \\
S_{j} = \left\{ x \in \mathbb{R}^{N} \middle| a_{j} \leq x \leq b_{j} \right\}.
\end{cases}$$
(21)

where each subregion S_j is defined by lower and upper bounds for the decision variables, and $a_j, b_j \in \mathbb{R}^N$ are the bounds for the j-th subregion. The optimization process begins by dividing the high-dimensional design space into a set of predefined subregions S_j through uniform grid partitioning. This involves segmenting each design variable's range into a specified number of equal intervals, thereby creating a grid of subregions that systematically covers the entire search space. Within each of these defined subregions, the NSGA-III algorithm is then applied

to generate and evolve populations, identifying Pareto-optimal solutions specific to that segment of the design space. Following this initial segmentation and exploration, an adaptive merging strategy, as detailed in Fig. 7, dynamically adjusts and combines these subregions. This merging mechanism, driven by the covariance of the Gaussian process surrogate models, allows for flexible redefinition of subregion boundaries based on the need for improved model accuracy and a more comprehensive representation of the overall solution landscape, particularly in promising areas. In each subregion S_i , a population P_i is first initialized with individuals $x \in P_i$ uniformly sampled from the subregion. The objective vector $F(x) = [f_1(x), ..., f_K(x)]$ for each individual is then evaluated. Subsequently, the individuals are ranked based on Pareto dominance using non-dominated sorting, where a solution x_1 dominates another x_2 if $f_1(x) \le f_K(x)$ for all $A_i = 1, 2, ..., K$, and $\exists_j : f_j(x_1) < f_j(x_2)$. This process forms successive Pareto fronts, with the first front containing the nondominated solutions, followed by subsequent fronts.

To maintain diversity, NSGA-III assigns each solution to a predefined reference point $Z_r \in \mathbb{R}^K$ in the objective space. For each individual, the perpendicular distance to the nearest reference point is calculated as follows

$$\min_{Z_r} \frac{|F(x) \cdot Z_r|}{|Z_r|},\tag{22}$$

ensuring that solutions are distributed uniformly along the Pareto front. Standard genetic operators, including simulated binary crossover (SBX) and polynomial mutation, are employed to produce offspring, promoting the exploration of new regions within the decision space. Over multiple generations, the population evolves towards a well-distributed Pareto front. Finally, after the termination criteria are met, the non-dominated set P_j^* is extracted as the Pareto-optimal solutions for the subregion S_i .

In the meantime, the optimization process in each subregion S_j generates a dataset $D_j = \left\{ \left(x^{(i)}, F(x^{(i)}) \middle| x^{(i)} \in P_j^* \right) \right\}$ of non-dominated

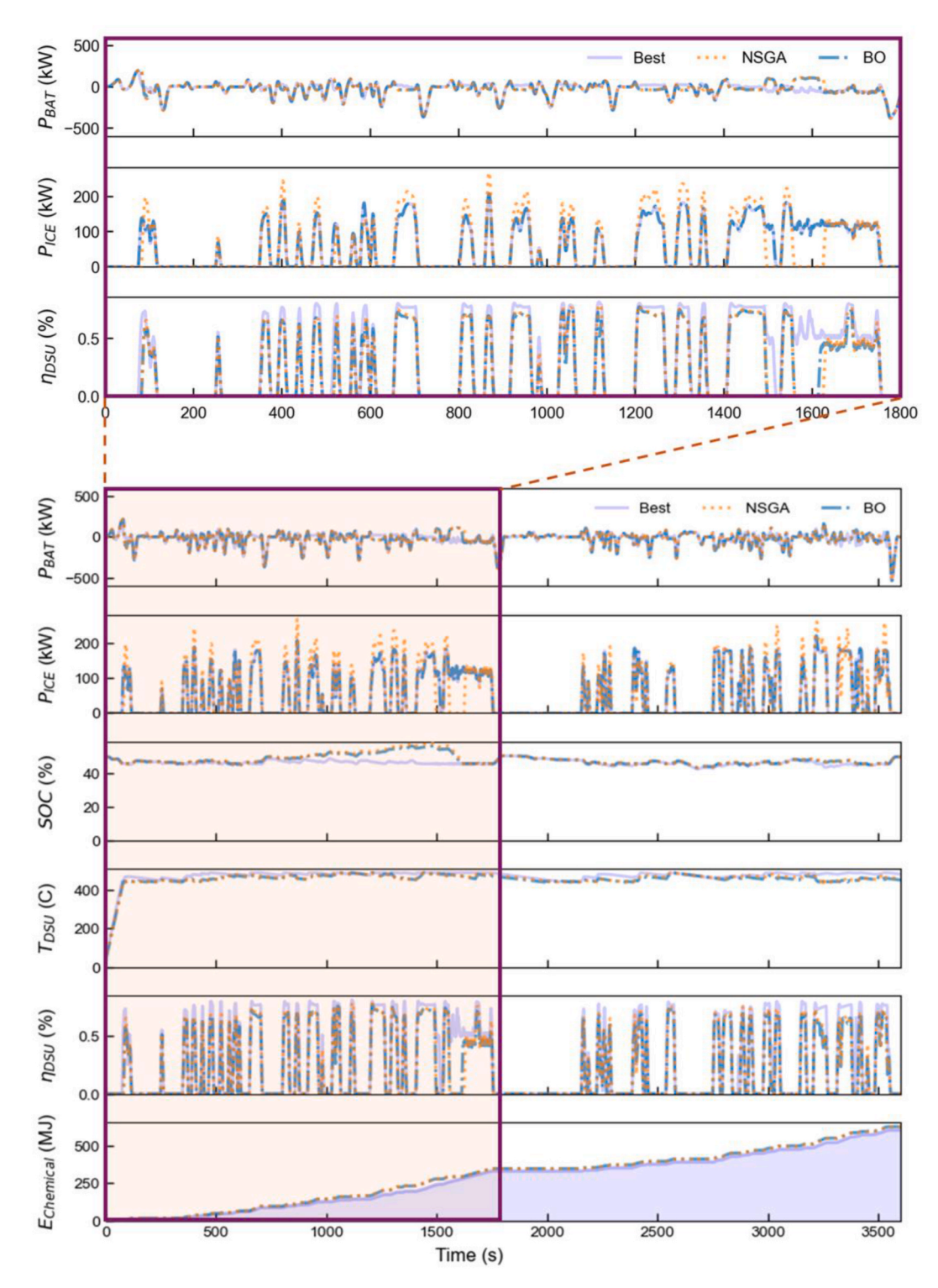


Fig. 14. Powertrain operation characteristics of the system under CHTC driving conditions.

solutions, which will be used to train surrogate models in the refinement phase. The accumulation continues until the solution density in S_j satisfies:

$$\frac{\left|P_{j}^{*}\right|}{\operatorname{vol}(S_{j})} > \rho_{\min}\left(\rho_{\min} = \varphi N_{d}\right) \tag{23}$$

where $vol(S_j)$ is the hypervolume of S_j , and φ is a coefficient adjusting the stop threshold, also, N_d refers to the dimension count.

3.3. Cross-region surrogate transfer and Bayesian refinement

The transition from global exploration to local refinement is governed by an adaptive data-driven mechanism. The refinement phase initiates by constructing GP surrogate models using the datasets D_j accumulated during NSGA-III optimization. A pivotal advantage is its ability to quantify prediction uncertainty, which is fundamental for efficiently guiding BO through balancing exploration and exploitation in high-dimensional spaces. Furthermore, GPs offer inherent flexibility for

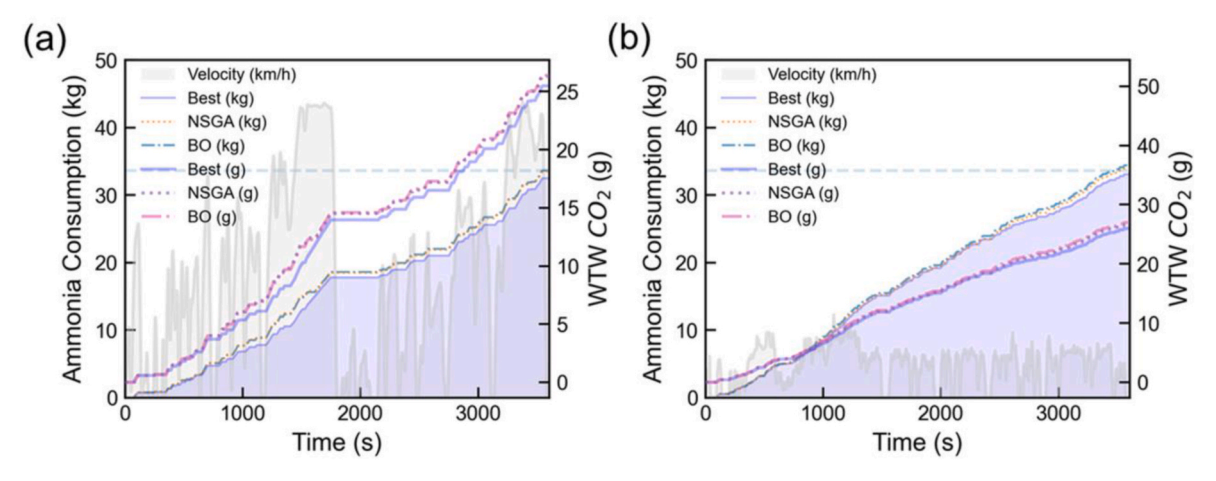


Fig. 15. Comparison of energy consumption and WTW CO2 emissions of different algorithms in the same driving cycle, (a) the standard cycle combined of CHTC and CWTVC, (b) the practice cycle of RD.

Table 7

Analysis of corrected energy consumption and WTW CO2 emission for different propulsion systems.

Driving cycle	Optimization (–)	Energy consumption (MJ/km)	WTW CO2 emission (kg CO2-eq/km)
Standard	Hybrid	604.08	25.49
driving cycle	NSGA-III	622.79	26.28
	BO	625.52	26.39
Real Driving	Hybrid	1184.21	49.97
Test Cycle	NSGA-III	1209.31	51.03
	BO	1228.54	51.84

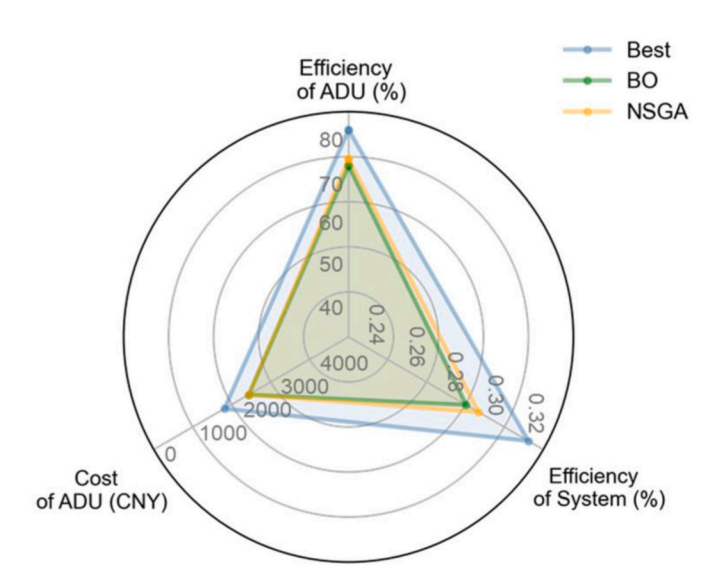


Fig. 16. Comparison of algorithms in system performance and cost.

capturing complex non-linear relationships and are data-efficient. This surrogate-assisted strategy enables the identification of promising adjacent subregions through solution space connectivity analysis. Specifically, neighboring subregions that exhibit solution clustering near their mutual boundaries are merged to form extended search spaces. Within these unified regions, BO initiates local refinement by strategically sampling points that simultaneously maximize the expected improvement (EI) acquisition function across all merged objectives, effectively bridging the gap between discrete Pareto fronts from separate subregions while preventing premature convergence. For each pair of

adjacent subregions S_j and S_{j+1} , their respective Pareto-optimal sets P_j^* and P_{j+1}^* are merged:

$$P_{merged} = \bigcup_{j=1}^{i-1} \left(P_j^* \bigcup P_{j+1}^* \right), \tag{24}$$

The merged Pareto set represents the combined non-dominated solutions near the boundaries of adjacent subregions. By merging adjacent Pareto fronts, we ensure that global interactions between neighboring regions are captured, leading to a more comprehensive search of the global Pareto front.

To enhance the quality of the merged Pareto fronts, BO is employed for global refinement. BO is particularly suited for expensive black-box optimization problems, leveraging a probabilistic surrogate model to balance exploration of the search space and exploitation of promising regions. The refinement process begins with constructing a GP surrogate model for each objective function using the dataset of solutions from the merged Pareto set, $D = \{(x_1, F(x_1)), ..., (x_n, F(x_n))\}$. The GP model is defined as

$$f_i(\mathbf{x}) \sim \mathscr{GP}(\mu_i(\mathbf{x}), k_i(\mathbf{x}, \mathbf{x}')),$$
 (25)

where $\mu_i(x)$ represents the mean function, and $k_i(x,x')$ is the covariance function. A commonly used kernel for the covariance function is the squared exponential kernel:

$$k_i(\mathbf{x}, \mathbf{x}') = \sigma_i^2 \exp\left(-\frac{1}{2l_i^2} ||\mathbf{x} - \mathbf{x}'||^2\right),$$
 (26)

where l_i denotes the characteristic length scale, and σ_i^2 represents the signal variance of the objective $f_i(x)$.

The next evaluation point is determined by optimizing an acquisition function α_x , which guides the selection by balancing exploration and exploitation. The expected improvement is a widely used acquisition function, defined as:

$$EI(x) = \mathbb{E}[max(0, f_{best} - f(x))]$$
(27)

where f_{best} is the best objective value observed so far, and f(x) is the predicted mean from the GP model. The next evaluation point x_{next} is obtained by maximizing the acquisition function:

$$x_{next} = \underset{x \in S}{\operatorname{argmax}} a_x, \tag{28}$$

The BO process iteratively updates the GP model with the new evaluations, refining the solutions at each step. This iterative process continues until convergence, which is defined when the maximum acquisition value satisfies the following

$$\max_{x} a(x) < \epsilon(\max(F) - \min(F))$$
 (29)

where ϵ is the relative convergence threshold, which ranges from 0 to 1. In addition, $\max(F)$ and $\min(F)$ are the maximum and minimum observed values of the objective functions, respectively.

During BO iterations, the GP models are continuously refined by incorporating newly evaluated points $(x_{new}, F(x_{new}))$ into the training dataset:

$$D_i \leftarrow D_i \cup \{(x_{new}, F(x_{new}))\},\tag{30}$$

which ensures that the surrogates progressively improve their accuracy in promising regions.

3.4. Settings of optimization variables

In this work, since P_{GEN}^{max} needs to match the engine requirement, which can be determined as a function of P_{ICE}^{max} . Therefore, the decision variables x include eight parameters related to the powertrain components that to be optimized, including ρ_{I}^{cat} , ρ_{II}^{cat} , ρ_{III}^{cat} , ρ_{IV}^{cat} , ρ_{ICE}^{cat} , P_{ICE}^{max} , P_{mot}^{max} and P_{Loc} .

Here, $\rho_{\mathrm{II}}^{\mathrm{cat}}$, $\rho_{\mathrm{III}}^{\mathrm{cat}}$, $\rho_{\mathrm{III}}^{\mathrm{cat}}$ and $\rho_{\mathrm{V}}^{\mathrm{cat}}$ refer to the proportion of the selected catalysts for the five catalyst pipes. It should be noted that the selection of catalyst type for each pipe could be the same. E_{bat} is the battery capacity in kWh. In the collaborative optimization process, it should be noted that the engine operates along the optimal operating line for simplicity.

The objective associated with system cost (f_2) is calculated based on the summation of the components cost denoted by f_2^{ICE} , f_2^{GEN} , f_2^{DM} , f_2^{bat} and f_2^{HPU} . The detailed parameters for calculating component cost of the engine, generator, motor, and battery are summarized in Table 4, and the calculation of the ADU cost with different catalyst design has been explained in Section II.

Table 5 outlines the multi-objective optimization framework, including specifics on the objective functions, variable ranges, and constraints. For powertrain optimization, this study employs a standardized driving cycle that integrates the China heavy-duty commercial vehicle test cycle (CHTC) with the Chinese-world transient vehicle cycle (CWTVC).

4. Results and discussions

4.1. Catalyst combination and Pareto surface optimization

The Pareto analysis-based optimization selects the combinations of catalysts for multi-objective optimization. The results of the modulation will be illustrated as follows: generations of distributions of the Pareto-based optimization, components of the selected catalyst combinations, performances of the selected catalyst combinations, and converging quality of Pareto throughout the generations. The analysis was employed to evaluate over 100 catalyst species and proportion combinations, which were initially selected from a larger set. These combinations underwent iterative optimization over successive generations with the goal of improving efficiency and reducing costs. The representative outcomes of this evolutionary optimization process are depicted in Fig. 8.

Table 6 demonstrates the most preferred combinations selected by the 60th generation of the best algorithm. In the 60th generation, the 10 coordinates closest to the Pareto surface were selected. The selected combination in Table 6 is the second among the 10 coordinates. The proportions of the five constituent species were analyzed and the two species with the lowest proportions were removed. The remaining percentage was then evenly redistributed among the three retained species. The proportion of eliminated species is illustrated in Fig. 9.

Fig. 10 displays the selected combinations under the optimal algorithm. The three graphs highlight different factors that influence these combinations. The higher the bars, the better the combinations. The left graph emphasizes cost, the center graph focuses on temperature, and the right graph highlights system efficiency. Convergence was assessed using the inverted generational distance (IGD) metric, as shown in Fig. 11 (a). The IGD value decreased rapidly from 0.0461 in the first generation to approximately 0.001 in the 60th generation, with the rate of decline slowing progressively over time. The best-performing algorithm achieved a minimum IGD of 0.000746. Beyond the 60th generation, no significant reduction in IGD was observed across any algorithm, indicating that further iterations would yield negligible improvement. Prior to the 17th generation, NSGA-BO required significantly more iteration time. However, upon conclusion of the NSGA exploration phase at the 17th generation, the computational time per generation for NSGA-BO exhibited a marked inflection point. The total computational time of NSGA-BO also fell below that of pure NSGA by approximately the 20th generation. Consequently, in achieving the best-performing algorithm of the 60th generation, NSGA-BO demonstrates clear advantages in time efficiency.

Furthermore, Fig. 11 (b) and Fig. 11 (c) illustrate the performance of the surrogate model. The scatter plot shows the relationship between the surrogate model outputs and the corresponding high-fidelity model outputs. The 45-degree line indicates perfect agreement between the two models, while the two red dashed lines represent a ± 10 % error margin. It can be observed that the surrogate model outputs closely follow those of the high-fidelity model, with most data points falling within the ± 10 % error range. The overall accuracy of the surrogate model is quantified by the R² value, which is 0.9774. The histogram depicts the distribution of errors between the surrogate and high-fidelity model outputs. The errors are centered around zero and show a relatively narrow spread in both directions, indicating that the surrogate model meets the required accuracy for the task. This work strategically terminated the optimization at the 60th generation as shown in Fig. 8 though the three algorithms may not have fully converged. By this point, the models' convergence rate have slowed significantly, and performance metrics IGD shown in Fig. 11 (a) confirmed our proposed NSGA-BO framework had already achieved a high-quality Pareto front. The primary objective was to demonstrate that our integrated NSGA-BO approach achieves superior solutions more rapidly than standalone methods. Continuing the optimization would have diminished the observable performance differences between algorithms, obscuring our method's core contribution. Thus, the results at 60 generations effectively showcase the framework's enhanced efficiency in achieving substantial progress in fewer generations.

To validate the robustness of our molecular dynamics model, sensitivity analysis is performed on the key parameters of system efficiency and ADU cost. Analysis for ADU efficiency is omitted as it should have similar sensitivity with system efficiency. 8 variables are considered in the examination for system efficiency: ρ_B^{cat} , ρ_D^{cat} , ρ_E^{cat} , ρ_G^{cat} , ρ_I^{cat} , P_{ICE} , P_{DM} , and E_{bat} . The results are shown in Fig. 12 (a). When each variable serves as the independent variable, it varies by \pm 15 %. When acting as control variables, P_{ICE} , P_{DM} and E_{bat} maintained within a fluctuation range of

 ± 2 %, ± 3 % and ± 5 % respectively. Catalysts ratio are considered in ADU cost sensitivity analysis as shown in Fig. 12 (b). Notably, ρ_E^{cat} contributes the highest effection on both system efficiency and ADU cost, suggesting the need for strict control in simulations. The significant influence of ρ_E^{cat} on the key parameters may stem from its consistently high prevalence across various catalyst combinations. These results confirm that our conclusions on grain boundary strengthening are insensitive to reasonable parameter variations.

The selected optimal catalyst combinations were applied to the ADU and powertrain model under various driving cycles, shown in Fig. 13. Three optimization algorithms were employed to refine vehicle parameters for multi-objective system optimization: BO, NSGA-III, and a

hybrid BO-NSGA-III approach. The hybrid method leveraged BO for local refinement and NSGA-III for global exploration, outperforming standalone algorithms in multi-aspect evaluations. Finally, Pareto-based multi-objective optimization was integrated with the hybrid strategy to identify catalyst combinations and proportions that best aligned with the target objectives.

Simulations were conducted using detailed engine, generator, motor, and battery parameters from Table 6, across three driving cycles: CHTC, CWTVC, and real driving (RD) test cycle. These cycles, along with acceleration-time profiles and acceleration-velocity gradients, are plotted in Fig. 13. The CHTC and CWTVC cycles are standardized for heavy-duty commercial vehicles and exclude real-world variables such as environmental conditions and driver behavior, which are incorporated into the RD cycle.

4.2. Comparison of Bayesian optimization and performance of NSGA-III

The dynamic performance analysis was performed on three optimization strategies, as shown in Fig. 14. BO demonstrated lower battery power consumption during driving cycles and achieved performance comparable to NSGA-III in engine power, SOC, ADU temperature, and energy cost. However, the hybrid BO-NSGA-III strategy outperformed both standalone methods, showing significant improvements in the ADU efficiency. Furthermore, the numerical information of accumulated energy consumption corresponding to Fig. 14, and the well-to-wheel (WTW) CO2 emission amount corresponding to Fig. 15 are summarized in Table 7.

To evaluate and compare algorithm performance, four metrics were analyzed: accumulated energy consumption (MJ), normalized energy consumption (%), ammonia consumption (kg), and well-to-wheel (WTW) CO2 emissions (kg). The total energy consumption values for the Best, NSGA-III, and BO algorithms were 604.08 MJ, 622.80 MJ, and 625.52 MJ, respectively. The normalized percentages of energy consumption were calculated by dividing the energy consumption of each algorithm by the total. Although BO and NSGA-III exhibited similar trends, the hybrid algorithm consistently demonstrated lower energy consumption throughout the timeframe, as shown in Fig. 15(a). This advantage becomes more pronounced in Fig. 15(b), where the finer y-axis scale reveals subtle yet significant differences in trends.

A comprehensive comparison of efficiency and cost for the ADU and powertrain system is summarized in Fig. 16. The hybrid optimization algorithm achieved the highest efficiency: 31.24 % for the powertrain system and 76 % for the ADU, along with the lowest cost of 1810 CNY for the ADU. In terms of the standalone methods, NSGA-III marginally outperformed BO in both efficiency and cost metrics.

5. Conclusions

This study addresses the critical challenge of optimizing ammonia decomposition catalysts for hydrogen production in carbon-free heavy-duty vehicles with the goal of balancing energy efficiency and system cost. The research focuses on identifying the optimal catalyst combinations and compositions to maximize ammonia conversion rates under lower temperature conditions, while minimizing preparation costs, thereby advancing the feasibility of ammonia-hydrogen hybrid power-trains. The key contributions of this study include:

- A dual-phase framework is proposed that combines genetic algorithm-based partitioned search with surrogate-guided refinement. This approach jointly explores component sizing and catalyst configurations, enabling efficient design of ammonia decomposition device for carbon-free powertrains under real-world dynamic operations.
- The proposed surrogate-assisted optimization integrates adaptive domain partitioning with Bayesian refinement, which eliminates premature convergence in nonconvex high-dimensional Pareto

- optimization and successfully coordinates powertrain parameters with catalyst composition variables through sequential domain decomposition and model-assisted merging.
- A dynamic simulation model is proposed that links catalyst properties with hybrid powertrains in real-world operation scenarios. The results validate the adaptability of the optimized catalyst combinations across driving cycles, with the proposed surrogate-enhanced dual-phase optimization strategy reducing energy consumption by 3.5 % compared with conventional NGSA-III and BO methods, and achieving 31.24 % powertrain efficiency and 76 % ADU efficiency with minimized system costs.

CRediT authorship contribution statement

Hao Zhang: Writing – original draft, Supervision, Methodology, Investigation, Conceptualization. Jiaxi Xu: Writing – original draft, Visualization, Validation, Software, Methodology. Nuo Lei: Validation, Software, Methodology, Investigation, Data curation. Bingbing Li: Writing – review & editing, Investigation, Data curation. Hao Sun: Software, Investigation, Data curation. Boli Chen: Writing – review & editing, Validation, Supervision, Funding acquisition, Conceptualization.

Declaration of competing interest

The authors declare that they have no known competing financial interests or personal relationships that could have appeared to influence the work reported in this paper.

Acknowledgments

This work was supported by the State Key Laboratory of Intelligent Green Vehicle and Mobility (Grant Number: KFZ2405). The authors would like to express their sincere gratitude to the China Scholarship Council for funding the research visit. This work was conducted by Dr. Hao Zhang (was a PhD student at Tsinghua University) and Dr. Bingbing Li (was a PhD student at Southeast University) during their CSC-sponsored research visit to Dr. Boli Chen's group at University College London. Special thanks are extended to Prof. Zhi Wang from Tsinghua University for his invaluable guidance in securing funding, as well as his insightful suggestions on the research topic and methodology.

Data availability

Data will be made available on request.

References

- Siong Chai Wai, Bao Yulei, Jin Pengfei, Tang Guang, Zhou Lei. A review on ammonia, ammonia-hydrogen and ammonia-methane fuels. Renew Sustain Energy Rev 2021;147:111254. https://doi.org/10.1016/j.rser.2021.111254. ISSN 1364-0321
- [2] Qiao Qingyao, Eskandari Hamidreza, Saadatmand Hassan, Ali Sahraei Mohammad. An interpretable multi-stage forecasting framework for energy consumption and CO2 emissions for the transportation sector. Energy 2024;286:129499. https://doi. org/10.1016/j.energy.2023.129499. SSN 0360-5442.
- [3] Aslan Alper, Ilhan Ozturk, Usama Al-Mulali, Savranlar Buket, Polat Melike Atay, Metawa Noura, Raboshuk Alina. Effect of economic policy uncertainty on CO2 with the discrimination of renewable and non renewable energy consumption. Energy 2024;291:130382. https://doi.org/10.1016/j.energy.2024.130382. ISSN 0360-5442.
- [4] Zhang Ying, Zahoor Zahid. The role of energy subsidies, savings, and transitions in driving energy transformations toward net-zero emissions. Energy 2025;320: 135209. https://doi.org/10.1016/j.energy.2025.135209. ISSN 0360-5442.
 [5] He Wei, King Marcus, Luo Xing, Dooner Mark, Li Dacheng, Wang Jihong.
- [5] He Wei, King Marcus, Luo Xing, Dooner Mark, Li Dacheng, Wang Jihong. Technologies and economics of electric energy storages in power systems: review and perspective. Adv Appl Energy 2021;4:100060. https://doi.org/10.1016/j. adapen.2021.100060. ISSN 2666-7924.
- [6] Li Wei, Wang Ting, Lu Can. Pathways to net-zero emissions from China's transportation industry: considering alternative fuels. Energy 2023;283:129059. https://doi.org/10.1016/j.energy.2023.129059. ISSN 0360-5442.

- [7] Zhang Dongfang, Sun Wei, Zou Yuan, Zhang Xudong, Zhang Yiwei. An improved soft actor-critic-based energy management strategy of heavy-duty hybrid electric vehicles with dual-engine system. Energy 2024;308:132938. https://doi.org/ 10.1016/j.energy.2024.132938. ISSN 0360-5442.
- [8] Guo Jun, Wu Jinglai, Zhang Yunqing, Peng Yayun. Driving mode shift strategy for an electric heavy truck to minimize the energy consumption and shift frequency. Energy 2025;319:134998. https://doi.org/10.1016/j.energy.2025.134998. ISSN 0360-5442.
- [9] Zhang Hao, Lei Nuo, Peng Wang, Li Bingbing, Li Shujun, Chen Boli, Wang Zhi. Bilevel transfer learning for lifelong intelligent energy management of electric vehicles. IEEE Trans Intell Transport Syst 2025. https://doi.org/10.1109/ TITS.2025.3571673. Early Access.
- [10] Tian Mei-Hui, Hu Yu-Jie, Li Chengjiang, Tao Yao, Wang Honglei. The development pathway for hydrogen fuel cell heavy duty trucks in China: an energy-environmenteconomy life cycle assessment approach. Energy 2025;322:135797. https://doi. org/10.1016/j.energy.2025.135797. ISSN 0360-5442.
- [11] Guo Xinpeng, Li Tie, Huang Shuai, Zhou Xinyi, Chen Run, Wei Wenze, Wu Zehao, Wang Ning, Li Shiyan. Characteristics of ignition, combustion and emission formation of premixed ammonia-hydrogen blends by hydrogen-fueled pre-chamber turbulent jets. Energy 2025;322:135573. https://doi.org/10.1016/j. energy.2025.135573. ISSN 0360-5442.
- [12] García Antonio, Monsalve-Serrano Javier, Martínez-Boggio Santiago, Wittek Karsten. Potential of hybrid powertrains in a variable compression ratio downsized turbocharged VVA Spark Ignition engine. Energy 2020;195:117039. https://doi.org/10.1016/j.energy.2020.117039. ISSN 0360-5442.
- [13] Zhang Hao, Lei Nuo, Wang Zhi. Ammonia-hydrogen propulsion system for carbon-free heavy-duty vehicles. Appl Energy 2024;369:123505. https://doi.org/ 10.1016/j.apenergy.2024.123505. ISSN 0306-2619.
- [14] Zhang Zhiqing, Hu Jingyi, Yang Dayong, Yin Zibin, Lu Kai, Tan Dongli. A comprehensive assessment over the environmental impact and combustion efficiency of using ammonia/hydrogen/diesel blends in a diesel engine. Energy 2024;303:131955. https://doi.org/10.1016/j.energy.2024.131955. ISSN 0360-5442
- [15] Chen Fujun, Wang Bowen, Ni Meng, Gong Zhichao, Jiao Kui. Online energy management strategy for ammonia-hydrogen hybrid electric vehicles harnessing deep reinforcement learning. Energy 2024;301:131562. https://doi.org/10.1016/ j.energy.2024.131562. ISSN 0360-5442.
- [16] Zhang Hao, Lei Nuo, Chen Boli, Li Bingbing, Li Rulong, Wang Zhi. Modeling and control system optimization for electrified vehicles: a data-driven approach. Energy 2024;310:133196. https://doi.org/10.1016/j.energy.2024.133196. ISSN 0360-5442.
- [17] Chamakhi Houda, Almusfar Latifa, Teka Hanen, Kouki Saoussen, Selmi Nadia, Elgarna Anis. United States transportation, economic growth, and CO2 emissions: a Kernel Transfer Entropy analysis. Energy 2025;322:135169. https://doi.org/ 10.1016/j.energy.2025.135169. ISSN 0360-5442.
- [18] Zheng Xiumin, Imran Muhammad, Umair Muhammad, Lin Chen, Dong Yue. Modern panelizing and optimization techniques for renewable energy projects; perspectives on how CO2 emissions impact the circular economy. Energy 2025; 323:135881. https://doi.org/10.1016/j.energy.2025.135881. ISSN 0360-5442.
 [19] Zhou Quan, Zhang Wei, Cash Scott, Olatunbosun Oluremi, Xu Hongming,
- [19] Zhou Quan, Zhang Wei, Cash Scott, Olatunbosun Oluremi, Xu Hongming, Lu Guoxiang. Intelligent sizing of a series hybrid electric power-train system based on Chaos-enhanced accelerated particle swarm optimization. Appl Energy 2017; 189-588-601. https://doi.org/10.1016/j.appergy.2016.12.074. ISSN 0306-2619.
- 189:588-601. https://doi.org/10.1016/j.apenergy.2016.12.074. ISSN 0306-2619. [20] Zhang Hao, Lei Nuo, Chen Boli, Li Bingbing, Li Rulong, Wang Zhi. Modeling and control system optimization for electrified vehicles: a data-driven approach. Energy 2024;310:133196. https://doi.org/10.1016/j.energy.2024.133196. ISSN 0360-5442
- [21] Zhang Hao, Chen Boli, Lei Nuo, Bingbing Li, Rulong Li, Wang Zhi. Integrated thermal and energy management of connected hybrid electric vehicles using deep reinforcement learning. IEEE Transactions on Transportation Electrification 2023. https://doi.org/10.1109/TTE.2023.3309396. 1-1.
- [22] Zhang Hao, Lei Nuo, Liu Shang, Fan Qinhao, Wang Zhi. Data-driven predictive energy consumption minimization strategy for connected plug-in hybrid electric vehicles. Energy 2023;283:128514. https://doi.org/10.1016/j. energy.2023.128514. ISSN 0360-5442.

- [23] Li Bingbing, Zhuang Weichao, Zhang Hao, Zhao Ruixuan, Liu Haoji, Qu Linghu, Zhang Jianrun, Chen Boli. A comparative study of energy-oriented driving strategy for connected electric vehicles on freeways with varying slopes. Energy 2024;289: 129916. https://doi.org/10.1016/j.energy.2023.129916. ISSN 0360-5442.
- [24] Ezzat MF, Dincer I. Development and assessment of a new hybrid vehicle with ammonia and hydrogen. Appl Energy 2018;219:226–39. https://doi.org/10.1016/ j.apenergy.2018.03.012. ISSN 0306-2619.
- [25] Zhai Lingling, Wong Chiu Shek, Zhang Honglei, Xiong Pei, Xue Xiangdang, Ho Yiu Lun, Xu Cuidong, Fong Yat Chi, Mei Jie, Chan Wing Wa, Ip Shu Chuen, Niu Shuangxia, Lau Shu Ping, Cheng Ka Wai Eric, Meng-Jung Li Molly. From lab to practical: an ammonia-powered fuel cell electric golf cart system. Chem Eng J 2023;452(Part 2):139390. https://doi.org/10.1016/j.cej.2022.139390. ISSN 1385-8947
- [26] Qi Yunliang, Liu Wei, Liu Shang, Wang Wei, Peng Yue, Wang Zhi. A review on ammonia-hydrogen fueled internal combustion engines. eTransportation 2023;18: 100288. https://doi.org/10.1016/j.etran.2023.100288. ISSN 2590-1168.
- [27] Lucentini Ilaria, Colli Germán García, Luzi Carlos D, Serrano Isabel, Martínez Osvaldo M, Llorca Jordi. Catalytic ammonia decomposition over Ni-Ru supported on CeO2 for hydrogen production: effect of metal loading and kinetic analysis. Appl Catal B Environ 2021;286:119896. https://doi.org/10.1016/j. apcatb.2021.119896. ISSN 0926-3373.
- [28] Yagmur Goren A, Temiz Mert, Erdemir Dogan, Dincer Ibrahim. The role of effective catalysts for hydrogen production: a performance evaluation. Energy 2025;315: 134257. https://doi.org/10.1016/j.energy.2024.134257. ISSN 0360-5442.
- [29] Zhang Ce, Dong Huijie, Xu Yuanlu, Nick Lucky. RETRACTED: balancing cost and efficiency: multi-objective optimization of battery-swapping stations for delivery vehicles. Energy 2024;309:133070. https://doi.org/10.1016/j. energy.2024.133070. ISSN 0360-5442.
- [30] Zhang Ce, Dong Huijie, Xu Yuanlu, Nick Lucky. Retraction notice to "Balancing cost and efficiency: multi-objective optimization of battery-swapping stations for delivery vehicles". Energy 309 (2024) 133070 Energy 2025;324:135896. https://doi.org/10.1016/j.energy.2025.135896. ISSN 0360-5442.
- [31] Li N, Zhang C, Li D, Jiang W, Zhou F. Review of reactor systems for hydrogen production via ammonia decomposition. Chem Eng J 2024;495:153125. https://doi.org/10.1016/j.cej.2024.153125.
- [32] Li J, Wang W, Chen W, Gong Q, Luo J, Lin R, Xin H, Zhang H, Wang D, Peng Q, Zhu W, Chen C, Li Y. Sub-nm ruthenium cluster as an efficient and robust catalyst for decomposition and synthesis of ammonia: break the "size shackles.". Nano Res 2018;11(9):4774–85. https://doi.org/10.1007/s12274-018-2062-4.
- [33] Xie P, Yao Y, Huang Z, Liu Z, Zhang J, Li T, Wang G, Shahbazian-Yassar R, Hu L, Wang C. Highly efficient decomposition of ammonia using high-entropy alloy catalysts. Nat Commun 2019;10(1). https://doi.org/10.1038/s41467-019-11848-
- [34] Xu K, Jiang N, Wang P, Wang W, Jia C. Highly efficient cobalt catalysts promoted by CeO2-Al2O3 for ammonia decomposition. Catal Sci Technol 2024. https://doi. org/10.1039/d4cv00835a.
- [35] Makepeace JW, Wood TJ, Hunter HMA, Jones MO, David WIF. Ammonia decomposition catalysis using non-stoichiometric lithium imide. Chem Sci 2015;6 (7):3805–15. https://doi.org/10.1039/c5sc00205b.
 [36] Liu H. Zhang R. Liu S. Liu G. CEO2/NI inverse catalyst as a highly active and stable
- [36] Liu H, Zhang R, Liu S, Liu G. CEO2/NI inverse catalyst as a highly active and stable RU-free catalyst for ammonia decomposition. ACS Catal 2024;14(13):9927–39. https://doi.org/10.1021/acscatal.4c02313.
- [37] Lucentini I, Casanovas A, Llorca J. Catalytic ammonia decomposition for hydrogen production on Ni, Ru and Ni Ru supported on CeO2. Int J Hydrogen Energy 2019; 44(25):12693–707. https://doi.org/10.1016/j.ijhydene.2019.01.154.
- [38] Akarçay Ö, Kurtoğlu SF, Uzun A. Ammonia decomposition on a highly-dispersed carbon-embedded iron catalyst derived from Fe-BTC: stable and high performance at relatively low temperatures. Int J Hydrogen Energy 2020;45(53):28664–81. https://doi.org/10.1016/j.ijhydene.2020.07.188.
- [39] Hu X, Wang R, Zhang G, Feng R. Ru/La2O3 catalyst for ammonia decomposition to hydrogen. Appl Surf Sci 2019;476:928–36. https://doi.org/10.1016/j. apsusc.2019.01.112.
- [40] Yaghobi Nakisa. The role of gas hourly space velocity and feed composition for catalytic oxidative coupling of methane: experimental study. J King Saud Univ Eng Sci 2013;25(1):1–10. https://doi.org/10.1016/j.jksues.2011.06.007. ISSN 1018-3639